J. Fluid Mech. (1988), *vol.* 197, *pp.* 201–240
Printed in Great Britain

On the stability of laminar boundary-layer flow over a flat plate with a compliant surface

By P. K. SEN AND D. S. ARORA
Department of Applied Mechanics, Indian Institute of Technology, New Delhi 110016, India

(Received 11 March 1986 and in revised form 17 May 1988)

The problem has been examined using a kinematic model for wall pliability, wherein a kinematic postulation of the wall boundary conditions is made. A form of the normalized wall-displacement and its phase are used as additional parameters in an extended eigenvalue problem. Using this technique the entire gamut of possibilities regarding stability of flow past (normally) pliable walls can be examined, yet without recourse to any specific material properties for the wall. Rather, the results based on the kinematic model can be used to back-calculate the material properties corresponding to any chosen model for the dynamics of the wall. A sample back calculation is discussed herein for the Benjamin–Landahl wall model, and based on this some predictions are made regarding both stabilization of the flow and physical realizability of modes. It is believed that the kinematic model will prove useful in further understanding of the problem, and in the design of stabilizing coatings.

The results show that there are three important 'mode classes' (distinct from 'modes'), namely the Tollmien–Schlichting (TS), resonant (R) and Kelvin–Helmholtz (KH). Whereas the TS and R mode classes broadly agree with modes bearing similar names as found by earlier workers, the present KH mode class is difficult to classify based on earlier work. Moreover, there are also important transitional mode classes in the regions of bifurcations of the regular mode classes.

Two important concepts evolve in connection with the TS and R mode classes, namely the existence of 'stable pockets' for the former and 'unstable pockets' for the latter. It is also confirmed herein that there are conflicting requirements on the damping d to stabilize TS and R modes. Considering these points it has been suggested that TS and R modes be avoided by keeping soft surfaces as compliant coatings. However, this in turn leads to instabilities from one of the transitional mode classes. It is also seen that a soft surface that is also marginally active (i.e. having a small negative value of d) could render even better stabilization.

1. Introduction

The interest in the problem of stability of laminar flow over a compliant surface was created mainly following Kramer's (1957, 1960*a*, *b*, 1965) extensive studies on the locomotion of dolphins and his reported experiment on drag reduction on a body of revolution covered with a designed compliant coating. The coating itself was backed up by a substrate fluid of high viscosity. Kramer called this technique stabilization by distributed damping, his basic hypothesis being that the viscosity of the substrate fluid would damp out any possible laminar instabilities in the flow. This would result in the delay of transition so that the boundary layer would remain laminar, and thus considerable drag reduction would be effected. This was also his

hypothesis to explain the apparent superiority in hydromechanical efficiency of a dolphin as compared to a manmade underwater projectile of similar displacement.

Following Kramer's work, the pioneering theoretical studies on the problem were done by Benjamin (1960, 1963) and Landahl (1962). This was followed by the works of Landahl & Kaplan (1965), Hains (1965) and others, and more recently by Carpenter & Garrad (1985, 1986). These works seem to have contradicted many of Kramer's surmises. Moreover, experiments have been carried out to seek independent confirmation of Kramer's results on drag reduction. These experiments seem not to have provided any confirmation of Kramer's results.

An excellent and succinct review of the past theoretical and experimental works has been given by Carpenter & Garrad (1985), who have also given a fairly exhaustive list of references. The reader is therefore referred to their paper for details in this respect. However, Carpenter & Garrad have pointed out that the experiments subsequent to Kramer's were not performed under quite the same conditions; therefore these later results neither prove nor disprove Kramer's original results. Carpenter & Garrad, on the basis of their theoretical investigations, also claim that it still might be possible to explain the successful drag reduction in Kramer's experiments and that 'Kramer-type coatings are theoretically capable of considerable transition postponement provided modal interaction does not occur'.

In the previous theoretical works, including that of Carpenter & Garrad, the basic flow considered is the boundary-layer flow over a flat plate. Almost all these works consider only normal pliability of the wall, the exception being Korotkin's (1965) work in which both normal and tangential compliancy are considered. Carpenter & Garrad point out that the no-slip condition has been apparently incorrectly implemented in Korotkin's work. Further, to the best of our knowledge, all the previous theoretical works consider the problem as a combined fluid–solid problem. This requires the separate specification of the dynamics of the fluid side and the solid side, and the matching of the two at the interface. The dynamics of the fluid side has been more or less standardized, in that the mean motion is described by the Blasius velocity profile, and the disturbances are described by the Orr–Sommerfeld equation. There is some margin for improvement in this area by considering non-parallel effects and boundary-layer growth. As regards the dynamics of the solid side, there has apparently been continual improvement over the simple stretched-membrane model postulated by Benjamin (1960) and Landahl (1962). For instance, in a recent model for the solid side, Carpenter & Garrad (1985) consider the dynamics of the substrate fluid and also the viscoelastic effects of the outer diaphragm and supporting stubs. In fact, there still remains a variety of choice in selecting a compliant layer according to one's own design, so that a variety of models may, in future, still be prescribed for the solid side. Consequently the study of the problem, as a combined fluid–solid problem, apparently still remains wide and open-ended. Moreover, the results obtained so far definitely do not point to a configuration that would guarantee stabilization, and consequent drag reduction, over a wide operational range. The problem therefore continues to remain very much unsolved, and perhaps a more basic understanding of it is necessary before the end can be foreseen.

It is in the context of the above background that the present method of analysis was conceived. It was felt that rather than specifying newer models for the compliant layer it would be more worthwhile to concentrate on the motion of the fluid–solid interface. Now, no matter what the nature of the compliant surface be, when a disturbance is present in the flowing fluid the interface will be correspondingly

disturbed from its stationary or mean position. Also, the normalized amplitude and phase of the displacement of the interface, relative to the disturbance in the flowing fluid, will depend on the actual nature of the backing compliant layer. To wit, different compliant layers will evoke different responses for the motion of the interface. Let us now reframe the problem in the following manner. Let the normalized displacement and phase of the interface by specified as additional parameters in an extended eigenvalue problem for the fluid side. This is tantamount to specifying boundary conditions on the moving boundary and considering the problem from the fluid side only. To begin with, the solid side, that is the backing compliant layer, is not in the picture at all. Nevertheless, if this extended eigenvalue problem is investigated for the entire possible range of values of the normalized displacement and phase of the interface, then the entire gamut of the problem will actually have been investigated. The last statement actually follows from the inversion of the earlier statement that different compliant layers will evoke different responses for the motion of the interface. Thus if all possible motion of the interface has been considered then it is tantamount to having considered all possibe backing compliant layers, in a combined fluid–solid problem.

We shall choose to call the present approach the 'kinematic model', partly to distinguish it from the earlier combined fluid–solid problems and partly because, in this model, the boundary conditions at the interface are kinematic. However, based on the results of the kinematic model, the material properties of the compliant layer, corresponding to any proposed design for the compliant layer, may be backcalculated.

2. Formulation

The problem may be formulated, as mentioned earlier, in two ways: as a combined fluid–solid problem as has been the approach in the earlier works; or by proposing (kinematic) boundary conditions at the interface and considering the problem from the fluid side only, as in the present kinematic model. It is necessary to clearly distinguish between these two approaches because initially the formulation is common to both, especially for the dynamics of the fluid side. We shall start with the common formulation, starting with the dynamics of the fluid side, and from the point where the formulations diverge two different approaches will be separately described.

The problem is considered with x and y as the coordinate axes respectively in the direction of flow and normal to the undisturbed fluid–solid interface. All quantities are normalized using the free-stream velocity U_∞ as the velocity scale and the boundary-layer thickness δ as the lengthscale. Further δ is defined as $\delta = 5(\nu x/U_\infty)^{\frac{1}{2}}$, and the mean-velocity distribution $U(y)$ is given by the Blasius velocity distribution. For simplicity non-parallel effects are ignored. The disturbance stream function $\psi(x, y, t)$, for an individual Fourier component, is given as

$$\psi(x, y, t) = A\phi(y)\, \mathrm{e}^{\mathrm{i}\alpha(x-ct)}, \tag{1}$$

where A is an arbitrary amplitude $O(\epsilon)$, $\phi(y)$ is the (complex) amplitude function assumed to depend on y only (since non-parallel effects are ignored) and ϕ is $O(1)$, α is the real spatial wavenumber and $c = c_\mathrm{r} + \mathrm{i}c_\mathrm{i}$ is the complex phase speed with c_r as the real phase speed and αc_i as the amplification factor of the disturbances. Also, only two-dimensional disturbances are considered after invoking Squire's theorem.

The equation for ϕ, for the linear theory, is given by the well-known Orr–Sommerfeld equation:

$$(U-c)(\phi''-\alpha^2\phi)-U''\phi+\frac{\mathrm{i}}{\alpha R}(\phi''''-2\alpha^2\phi''+\alpha^4\phi)=0, \tag{2}$$

where the Reynolds number $R = U_\infty \delta/\nu$, and primes denote differentiation with respect to y. The boundary conditions at the outer edge of the boundary layer may be reduced to the following form (see Schlichting 1968):

$$\Phi = \phi'+\alpha\phi = 0, \quad y \geqslant 1, \tag{3}$$

which is the same as in the rigid-wall case. Carpenter & Garrad (1985) have given an improved version of the outer boundary conditions. However if (3) is applied at $y \geqslant 1.5$ the level of accuracy in the numerical work remains adequate.

The boundary conditions at the wall, for the rigid-wall case and for different versions of the pliable-wall problem, will obviously be different. For the rigid-wall case these are given as

$$\phi = 0, \quad \phi' = 0, \quad y = 0. \tag{4}$$

With the Orr–Somerfeld equation (2), and the boundary conditions (3) and (4), an eigenvalue problem in α, c and R is obtained for the rigid-wall case.

The boundary conditions for the pliable wall require some care in description, especially to distinguish between the two approaches mentioned earlier in formulating the problem. At the outset we assume that the wall is pliable only in the normal (y-) direction and that there is no motion of the wall in the tangential (x-) direction. The displacement y_s of the interface, from its stationary or mean position, may be given in either of the two approaches as

$$y_s = Aa\, \mathrm{e}^{\mathrm{i}\alpha(x-ct)}, \tag{5}$$

where a is a non-normalized form of the amplitude of the wall displacement and is $O(1)$. It is important to remember that although a is $O(1)$, it continues to remain arbitrary unless a normalization is specified for ϕ. Upon equating the normal velocities of the fluid and the solid at the wall one obtains

$$\phi = ac, \quad y = 0, \tag{6}$$

where the term 'wall' means the position $y = 0$, that is the undisturbed position of the interface. Also the tangential no-slip condition at the interface, after linearization, yields the following equation:

$$\phi' = -aU'_{\mathrm{w}}, \quad y = 0, \tag{7}$$

where subscript w refers to the wall. Linearization is justified since A is $O(\epsilon)$.

This is the point at which the description of the problem begins to differ for the two approaches. Each approach is described separately below.

2.1. *The combined fluid–solid model*

In this approach, initiated by Benjamin (1960) and Landahl (1962), first (6) and (7) are combined to eliminate a. This gives

$$c\phi'+U'_{\mathrm{w}}\phi = 0, \quad y = 0, \tag{8}$$

and (8) is used as one of the wall boundary conditions. The second boundary condition at the wall is obtained by equating at the wall the wall pressures, or a

pressure-derived response coefficient like admittance, calculated respectively from the fluid side and from the solid side. The wall pressure p_w may be defined as

$$p_w = A\hat{p}_w \, e^{i\alpha(x-ct)}, \tag{9}$$

where $\hat{p}_w$ is the amplitude of the wall pressure and is $O(1)$. From the fluid side, two alternative expressions may be given for $\hat{p}_w$ based respectively on the x- and y-momentum equations, which are respectively

$$\hat{p}_w = \frac{i}{\alpha R}(\phi'''_w - \alpha^2\phi'_w), \tag{10}$$

$$\hat{p}_w = \alpha^2 \int_0^\infty \left(U - c - \frac{i\alpha}{R}\right)\phi \, dy - \frac{i\alpha\phi'_w}{R}, \tag{11}$$

It should be noted from (10) and (11) that the value of $\hat{p}_w$ depends on the normalization of ϕ. Landahl employed the concept of admittance defined as minus the ratio of the wall velocity to the wall pressure. From the fluid side the admittance Y is given as

$$Y = \frac{i\alpha\phi}{\hat{p}_w}, \quad y = 0, \tag{12}$$

where either of the expressions (10) or (11) could be used for $\hat{p}_w$ in (12). It should be noted from (12) that since ϕ and $\hat{p}_w$ appear in ratio form, Y is independent of the normalization for ϕ.

We next consider the solid side. The simple stretched-membrane model with inertia and damping, proposed by Benjamin (1960) and Landahl (1962), has the added merit that more complicated models may be reduced to an equivalent model. In certain respects this helps in obtaining a better physical understanding of the problem as will be seen later herein. The differential equation describing the motion of a stretched membrane is given as

$$m\frac{\partial^2 y_s}{\partial t^2} - T\frac{\partial^2 y_s}{\partial x^2} + \bar{d}\frac{\partial y_s}{\partial t} = -p_w, \tag{13}$$

where m, T and $\bar{d}$ are respectively the mass per unit area, longitudinal tension per unit width and damping, in suitable non-dimensional form. Using (5) and (9) in (13) an alternative expression for $\hat{p}_w$ is obtained from the solid side. If this is substituted in (12), in conjunction with (6), an alternative expression for the admittance is obtained from the solid side. Calling the later Y_0, the expression for Y_0 is given as

$$Y_0 = -\frac{ic}{m\alpha\left(c_0^2 - c^2 - \frac{icd}{\alpha}\right)}, \tag{14}$$

where c_0 is the surface wave speed given as $c_0 = (T/m)^{\frac{1}{2}}$, and $d = \bar{d}/m$. Thereafter the second boundary condition at the wall, in the combined fluid–solid model, is given as

$$Y - Y_0 = 0, \quad y = 0, \tag{15a}$$

which is analogous to the condition given by Hains (1965), i.e.

$$\zeta\phi''' + \phi = 0, \tag{15b}$$

where ζ is a parameter involving m, T and d.

Thus in the combined fluid–solid problem the basic Orr–Sommerfeld equation (2), along with boundary conditions (3), (8) and (15*a*) (or (15*b*)), constitutes a homogeneous eigenvalue problem. In this problem m, T and d are additional parameters, and the combined effect of these appears through Y_0 or ζ.

As regards the more recent models for the combined fluid–solid problem, cf. Carpenter & Garrad's model, the following observations are pertinent in relation to interpretation of certain results based on the kinematic model. Despite increased sophistication, these models can be reduced to an equivalent Benjamin–Landahl form. For example Carpenter & Garrad include in their model the flexural-rigidity term B, the spring-stiffness term K and the buoyancy effect of the substrate fluid. The buoyancy term modifies K to $K_e = K - g(\rho - \rho_s)$, where ρ is the density of the upper fluid and ρ_s that of the substrate fluid. With these additions c_0^2 in (14) is modified to an equivalent $\bar{c}_0^2$ in the following manner:

$$\bar{c}_0^2 = c_0^2 + \frac{B}{m}\alpha^2 + \frac{K_e}{m}\alpha^{-2}. \tag{16}$$

Further, Carpenter & Garrad consider the effect of the pressure p_s of the substrate fluid. For small depths of the substrate fluid this acts like the conventional damping term, so that d may be suitably modified in (14). When the small substrate depth assumption cannot be made the full expression for p_s, as given by Carpenter & Garrad (1985), has to be retained in (14). The viscoelastic effects of the diaphragm material and supporting stubs are also considered by Carpenter & Garrad. In relation to (14), all these added effects may be lumped into two parts: one modifying the real part of the denominator in (14), that is modifying c_0^2 (similarly as in (16)); and the second part modifying the imaginary part of the denominator in (14), that is modifying d. This would mean that c_0^2 and d will no longer be constant but will depend on α, and the other material and physical properties of the composite compliant layer.

We would like to retain the simple Benjamin–Landahl expression as in (14), since this form proves to be useful in interpreting results based on the present kinematic model. This is especially so because the other more complex models can, generally speaking, be reduced to an equivalent Benjamin–Landahl form for each fixed α.

2.2. *The kinematic model*

In this approach also the outer boundary condition is given by (3). At the wall the boundary conditions are given by (6) and (7), so that the wall boundary conditions are explicitly inhomogeneous. Although solutions may be obtained for (2) with boundary conditions (3), (6) and (7), the formulation of the problem is still not in a form that is convenient enough. To examine this point we look at the formal solution of (2) in terms of the four fundamental solutions of the Orr–Sommerfeld equation, viz. ϕ_ν, $\nu = 1, 2, 3, 4$ (see Schlichting 1968). Of these ϕ_1 and ϕ_2 are the inviscid solutions and ϕ_3 and ϕ_4 are the viscous solutions. ϕ_4 grows away from the wall and is discarded. Using ϕ_1, ϕ_2 and ϕ_3, and boundary conditions (3), (6) and (7), the following characteristic equations are obtained:

$$C_1 \Phi_{1d} + C_2 \Phi_{2d} = 0, \tag{17a}$$

$$C_1 \phi_{1w} + C_2 \phi_{2w} + C_3 \phi_{3w} = ac (= \phi_w), \tag{17b}$$

$$C_1 \phi'_{1w} + C_2 \phi'_{2w} + C_3 \phi'_{3w} = -aU'_w \left(= -\frac{U'_w \phi_w}{c} \right), \tag{17c}$$

where $\Phi_{vd} = \phi'_{vd} + \alpha\phi_{vd}$, subscript w refers to the undisturbed position of the wall, and subscript d refers to a chosen fixed point in the region $y \geqslant 1$, where $y = 1$ is the boundary-layer thickness. Also, C_1, C_2 and C_3 are constants to be determined from the simultaneous solution of (17*a–c*).

We examine the solutions of (17*a–c*) for a fixed α and R, remembering that α is arbitrary. For any particular choice of c with $c \neq \bar{c}$, where $\bar{c}$ is a rigid-wall eigenvalue, it is seen from (17*a–c*) that a family of solutions is obtained for ϕ. This is defined as $\phi(a, c) = a\phi(1, c)$ where $\phi(1, c)$ is the solution corrsponding to $a = 1$ and the chosen value of c. Now, each different choice of c gives a different family of solutions, and therefore, to eliminate unnecessary multiplicity we consider only one member from each family of solutions, that is a suitable normalized member. Let the normalized member be called $\bar{\phi}$, that is distinguished by an overbar from the rest of the members of the family, and let a chosen normalization be $\bar{\phi}_d = 1$. With this choice, the solution for $\bar{\phi}$ becomes unique, and for a fixed α and R, $\bar{\phi}$ depends only on the choice of c. Consequently $\bar{\phi}_w$ is unique and depends only on the choice of c. We may also write another important equation analogous to (6):

$$\bar{\phi}_w = \bar{a}c, \tag{18}$$

where, unlike in (6) where a is arbitrary, the *normalized* amplitude $\bar{a}$, of the wall displacement, is fixed. At this stage the proposition of the problem may be inverted. For a fixed α and R we can introduce $\bar{\phi}_w$ as an additional parameter, and the value of $\bar{\phi}_w$ is specified by choice. Thereafter one may endeavour to determine the compatible value of c that will satisfy the following characteristic equations:

$$\bar{C}_1\phi_{1d} + \bar{C}_2\phi_{2d} = 1, \tag{19a}$$

$$\bar{C}_1\Phi_{1d} + \bar{C}_2\Phi_{2d} = 0, \tag{19b}$$

$$\bar{C}_1\phi_{1w} + \bar{C}_2\phi_{2w} + \bar{C}_3\phi_{3w} = \bar{\phi}_w (= \bar{a}c), \tag{19c}$$

$$\bar{C}_1\phi'_{1w} + \bar{C}_2\phi'_{2w} + \bar{C}_3\phi'_{3w} = -\frac{U'_w\bar{\phi}_w}{c} \left(= -\bar{a}U'_w\right), \tag{19d}$$

where overbar in $\bar{C}_i$ is to distinguish from the C_i in (17*a–c*). Note that (19*a*) is a mandatory condition that follows from the definition of $\bar{\phi}$, i.e. $\bar{\phi}_d = 1$ at $y = d$, with $d \geqslant 1$. The compatible value of c in (19*a–d*) may be determined by solving the determinant given below, which follows from the solvability condition of (19*a–d*):

$$\begin{vmatrix} \phi_{1d} & \phi_{2d} & 0 & -1 \\ \Phi_{1d} & \Phi_{2d} & 0 & 0 \\ \phi_{1w} & \phi_{2w} & \phi_{3w} & -\bar{\phi}_w \\ \phi'_{1w} & \phi'_{2w} & \phi'_{3w} & \dfrac{U'_w\bar{\phi}_w}{c} \end{vmatrix} = 0. \tag{20}$$

We shall now endeavour to show that the problem formulated above has the features of an eigenvalue problem in α, R, c and $\bar{\phi}_w$ and thus may be called a modified or extended eigenvalue problem, although the boundary conditions are inhomogeneous. However, for brevity, we shall refer to the compatible value of c in (20) as the 'eigenvalue' for c. For chosen α, R and $\bar{\phi}_w$ let a typical eigenvalue for c in (20) be given as $c = c^*$. We notice first that $\bar{a}$ is determined from (18) as $\bar{a} = \bar{\phi}_w/c^*$. Further, upon substituting $c = c^*$ in (17*a*, *b*, *c*) the family of solutions corresponding to $c = c^*$ may be obtained. We notice that $C_i = \lambda\bar{C}_i$, subject to $c = c^*$,

where $\lambda = a/\bar{a}$. Since a is a free constant there is no restriction on the value of λ, and the family of solutions for ϕ is given as $\phi = \lambda\bar{\phi}$. It may be noted that the trivial solution for ϕ also exists, which is obtained by letting $\lambda = 0$. Thus each family of solutions for ϕ has all the attributes that go with an eigensolution, although to arrive at a particular family of solutions for ϕ, and to pose the problem on lines parallel to a conventional eigenvalue problem, we have to introduce $\bar{\phi}$ and consider $\bar{\phi}_w$ as an additional specifiable parameter. Thus for a fixed α and R, ϕ is characterized as $\phi = \phi(\bar{\phi}_w, c^*)$.

There are also a few other points worthy of note. First, in place of $\bar{\phi}_w$, the normalized amplitude of the wall displacement $\bar{a}$ could also have been used as a parameter in the eigenvalue problem, in which case $\bar{\phi}_w$ would have been determined *a posteriori* from (18), and, in (20) $\bar{\phi}_w$ would have had to be replaced by $\bar{a}c$. Secondly, $\bar{\phi}_w$ or $\bar{a}$ represents a rational departure from rigidity in the sense that as $\bar{\phi}_w \to 0$ (or $\bar{a} \to 0$), $c^* \to \bar{c}$, where $\bar{c}$ is the rigid-wall eigenvalue. Thus $\bar{\phi}_w$ and $\bar{a}$ are both $O(\delta c)$ where $\delta c = c^* - \bar{c}$. Incidentally (20) also reduces to the characteristic determinant for the rigid-wall case when $\bar{\phi}_w \to 0$. Thirdly, in the general scheme of things, the rigid-wall eigenvalue problem may be considered as a special case of the present problem with $\bar{\phi}_w = 0$, and the rigid-wall eigensolution for ϕ has the same attributes for ϕ as mentioned earlier, viz. $\phi = \lambda\bar{\phi}$ and that the trivial solution exists. However, although λ is arbitrary here as well, λ cannot be put as $\lambda = a/\bar{a}$ since $\bar{a} = 0$ for the rigid-wall case.

The discussions above give a formal basis for the kinematic model. Operationally speaking this model is an extended eigenvalue problem in α, R, c and $\bar{\phi}_w$ (or $\bar{a}$). After choosing α, R and $\bar{\phi}_w$, one has to determine the eigenvalue c, and the *normalized* eigensolution $\bar{\phi}$. Further, upon using $\bar{\phi}$ in (10) or (11) the wall pressure amplitude $\hat{p}_w$ is obtained, but now the value of $\hat{p}_w$ is definite since $\bar{\phi}$ is already normalized. Moreover the admittance Y, from the fluid side, may be obtained from (12) and as mentioned earlier the value of Y is independent of the normalization for ϕ.

The main advantage of the kinematic model is that the stability of the flow can be studied from the fluid side only after properly choosing an additional parameter $\bar{\phi}_w$ or $\bar{a}$ to typify the motion of the interface. Secondly the results based on the kinematic model, like $\hat{p}_w$ or Y, can be used to back calculate the material properties of the backing compliant layer. Thirdly, as mentioned earlier, if an exhaustive range of values of the parameter $\bar{\phi}_w$ or $\bar{a}$ is chosen, then the entire gamut of the problem will actually have been investigated, yet without reference to the material properties of the wall.

3. Numerical methods

The mean velocity of the flow was obtained from Blasius's solution using a Runge–Kutta scheme of integration. For the solution of the Orr–Sommerfeld equation a finite-difference procedure was used. This was the same as Thomas's (1953) method for the rigid-wall case. For the pliable-wall case extensions of Thomas's method were developed. The rigid-wall problem is homogeneous and the determinant of the coefficient matrix has to be zero in a finite-difference solution scheme. In fact this condition enables one to determine the eigenvalue in the rigid-wall case. The matrix representation of the finite-difference solution is

$$[A_{ij}][g_j] = [P_i], \quad i,j = 1,2,\ldots,N+1, \tag{21}$$

where $[A_{ij}]$ is a pentadiagonal band matrix, $[g_j]$ is a column vector of Thomas's auxilliary function (actually a Noumerov-type transform of the discretized ϕ-function), and $[P_i]$ is the right-hand-side column vector. Also $i = 1$ corresponds to $y = 0$ and $i = N+1$ corresponds to $y = d$, where N is the number of steps in the finite-difference procedure. As mentioned earlier all the $P_i = 0$ for the rigid-wall case. However, for the pliable-wall case, in view of (6) and (7), P_1 and P_2 are non-zero and both contain a (*vide* (6) and (7)) as a multiplying factor. But, the coefficient matrix $[A_{ij}]$ remains the same as in the rigid-wall case. Now for a given α and R, any choice of c with $c \neq \bar{c}$, where $\bar{c}$ is a rigid-wall eigenvalue, ensures that $\det[A_{ij}]$ is non-zero, in which case there is no difficulty in solving (21), and the solution for $[g_j]$, and consequently $[\phi_j]$, contains a as an arbitrary multiplying factor. The solution for ϕ can be made unique by specifying a normalization, like $\phi = 1$ at $y = d$ with d as a chosen fixed point in $y \geqslant 1$. This step actually gives us the normalized solution $\bar{\phi}$ from which a value for $\bar{\phi}_w$ is obtained.

In the kinematic model the value of $\bar{\phi}_w$ is specified by choice along with α and R. Thus to obtain the eigenvalue for c in the kinematic model, c is successively adjusted, and the solution for (21) repeated, until the difference between the specified value of $\bar{\phi}_w$ and the value of $\bar{\phi}_w$ obtained from the latest solution of $\bar{\phi}$, becomes insignificant.

In the combined fluid–solid models, for a chosen α and R and a trial value of c, first the admittance Y_0 (see (14)) from the solid side is evaluated. Secondly the solution for (21) is obtained, from which the admittance Y from the fluid side is evaluated. To get the eigenvalue of c, the value of c is continually adjusted, and the evaluation of Y_0 and Y repeated, until the difference between Y_0 and Y becomes significant.

Both the procedures described above are remarkably simple, and in both the result for the eigenvalue c converges rapidly upon using a two-dimensional Newton–Raphson technique. The accuracy is as good as in Thomas's method for the rigid-wall case, i.e. errors are $O(h^4)$ where h is the step size. The calculations were performed on an ICL-2960 computer using double-precision arithmetic.

4. Some predictions based on the formal solution and related results

4.1. *Comparison with Benjamin's formal solution*

The formal solution for the kinematic model is embodied in (20). Before making any predictions based on this it is worth comparing the solution with Benjamin's (1960) formal solution for the pliable wall. Broadly speaking there is a conceptual similarity between (20) and Benjamin's eigenvalue problem for the pliable wall (Benjamin 1960, eqs. (3.1)–(3.4)), to the extent that Benjamin also does not introduce wall material properties beforehand. Rather he introduces a surface compliance Λ (α in Benjamin's notation; also see eqn. (3.2) in Benjamin 1960) as a parameter defined as

$$\Lambda = \frac{U'_w \phi_w}{\hat{p}_w}, \tag{22}$$

and we see from (12) that Λ is closely related to the admittance Y. Also, like Y, Λ is independent of the normalization for ϕ. Thus, without loss of generality, we may assume that $\Lambda = U'_w \bar{\phi}_w / \hat{p}_w$, with $\hat{p}_w$ evaluated based on $\bar{\phi}$. Thereafter it is seen from (20) that there is a unique mathematical correspondence between Λ and $\bar{\phi}_w$. Moreover, it will be shown later that for low $\bar{\phi}_w$-modes (to be defined subsequently), and particularly for the Tollmien–Schlichting type modes, $\hat{p}_w$ is approximately a real

constant for a fixed α and R. In such a situation Λ is almost a (real) constant times $\bar{\phi}_w$.

We thus see that in Benjamin's eigenvalue problem also, Λ is effectively like a 'kinematic parameter' similar to $\bar{\phi}_w$, in the sense that wall material properties need not be initially introduced in Λ. The point of departure from Benjamin's analysis of the present one is in the manner in which the respective eigenvalue problems are tackled and in the type of end results in view. We discuss Benjamin's analysis first.

The classical Tollmien–Schlichting eigenvalue problem for the rigid wall reduces to the following characteristic equation:

$$F(z) = E(\alpha, c), \tag{23}$$

where $F(z)$ is called the Tietjen's function defined in terms of the viscous solution ϕ_3 with $z = (\alpha R U'_c)^{\frac{1}{3}} y_c$, and, $E(\alpha, c)$ is the inviscid part dependent on the inviscid solutions ϕ_1 and ϕ_2. Subscript c refers to the critical point. For simplicity Benjamin chose the variable z as $z = (\alpha R U'_w)^{\frac{1}{3}} c/U'_w$, after using the approximations $U'_w \approx U'_c$ and $y_c \approx c/U'_w$. Thereafter he obtained the pliable-wall characteristic equation as

$$F(z) = \frac{E + \Lambda(1-E)}{1 + \Lambda(1-E)} = E_1(\alpha, c). \tag{24}$$

Thus a very elegant connection was established between the rigid-wall and pliable-wall characteristic equations, respectively (23) and (24); and Benjamin was able to show that the rigid-wall neutral curve will shift in the (α, R)-plane accordingly as the pair (α, c) transforms to the pair (α_1, c_1) so as to make $E(\alpha, c) = E_1(\alpha_1, c_1)$. However, the qualitative predictions regarding shift of the neutral curve that Benjamin actually made, were done only after introducing the wall material properties. In essence therefore it was probably not Benjamin's intention to utilize the parameter Λ independent of the wall material properties. Moreover, despite its elegance (24) has certain limitations. First, the expression $z = (\alpha R U'_w)^{\frac{1}{3}} c/U'_w$ is too approximate for accurate quantitative work. Secondly, as mentioned by Benjamin himself, (23) and (24) refer only to Tollmien–Schlichting type modes, and (24) does not cover the various other modes that appear in the pliable-wall problem. Thirdly, the characteristic equation (23), and therefore (24) also, are ueful only for near-neutral disturbances. We may thus state in conclusion that although conceptually speaking the parameter Λ of Benjamin is as general as the parameter $\bar{\phi}_w$ used in the present kinematic model, his formal solution (24) can give results that are subject to the above restrictions and limitations. We next look at the kinematic model.

4.2. *The behaviour of Tollmien–Schlichting-type modes as predicted by the kinematic model*

Certain predictions may also be made based on the formal solution (20) for the kinematic model. Unlike Benjamin's work where the aim was mainly to study the shift in the rigid-wall neutral curve, in the present kinematic model the aim is to see what is happening at a particular point in the (α, R)-plane with change in the pliability of the wall.

The determinant in (20) may be expanded to the following form:

$$\Delta + \bar{\phi}_w \Delta_1 \left(\phi'_{3w} + \frac{U'_w}{c} \phi_{3w} \right) = 0, \tag{25}$$

where Δ is the determinant corresponding to the rigid-wall case, given as

$$\Delta = \begin{vmatrix} \Phi_{1d} & \Phi_{2d} & 0 \\ \phi_{1w} & \phi_{2w} & \phi_{3w} \\ \phi'_{1w} & \phi'_{2w} & \phi'_{3w} \end{vmatrix}, \tag{26}$$

and Δ_1 is the following determinant:

$$\Delta_1 = \begin{vmatrix} \phi_{1d} & \phi_{2d} \\ \Phi_{1d} & \Phi_{2d} \end{vmatrix} = \begin{vmatrix} \phi_{1d} & \phi_{2d} \\ \phi'_{1d} & \phi'_{2d} \end{vmatrix}. \tag{27}$$

Let the rigid-wall eigenvalue for a given α and R be $\bar{c}$, in which case the pliable-wall eigenvalue c, for limiting departures from rigidity, will be given as $c = \bar{c} + \delta c$. Such modes will be referred to as the Tollmien–Schlichting type (TS) modes. We remember that $\bar{\phi}_w$ is $O(\delta c)$ and that as $\bar{\phi}_w \to 0, c \to \bar{c}$, and it follows from (25) and (26) that $\Delta \to 0$. Thus for limiting departures from rigidity (25) reduces to

$$\left[\left(\frac{\partial \Delta}{\partial c}\right)_{c=\bar{c}} \delta c\right](\bar{c} + \delta c) = -\bar{\phi}_w \Delta_1[(\bar{c} + \delta c)\phi'_{3w} + U'_w \phi_{3w}]. \tag{28}$$

Upon retaining highest order $O(\delta c)$ terms in (28) the following equation is obtained:

$$\delta c = -\bar{\phi}_w \lambda, \tag{29}$$

where λ is a complex constant evaluated at $c = \bar{c}$, given as

$$\lambda = \left[\frac{\Delta_1(\bar{c}\phi'_{3w} + U'_w \phi_{3w})}{\partial \Delta / \partial c\, \bar{c}}\right]_{c=\bar{c}}. \tag{30}$$

Putting $\bar{\phi}_w$ and λ respectively as $\bar{\phi}_w = |\bar{\phi}_w| e^{i\theta}$ and $\lambda = |\lambda| e^{i\theta_c}$, we may separate the real and imaginary parts of δc to get

$$\delta c_r = -|\bar{\phi}_w| |\lambda| \cos(\theta + \theta_0), \tag{31}$$

$$\delta c_i = -|\bar{\phi}_w| |\lambda| \sin(\theta + \theta_0), \tag{32}$$

Thus, remembering that $c_r = \bar{c}_r + \delta c_r$ and $c_i = \bar{c}_i + \delta c_i$, we note that c_r and c_i vary as sinusoids with the phase angle θ of $\bar{\phi}_w$, and with the rigid-wall values $\bar{c}_r$ and $\bar{c}_i$ respectively as mean values. Moreover the normalized quantities $\delta c_r/|\bar{\phi}_w|$ and $\delta c_i/|\bar{\phi}_w|$ should vary only with θ, and the respective expressions are given as

$$\frac{\delta c_r}{|\bar{\phi}_w|} = -|\lambda| \cos(\theta + \theta_0), \tag{33}$$

$$\frac{\delta c_i}{|\bar{\phi}_w|} = -|\lambda| \sin(\theta + \theta_0), \tag{34}$$

Typical results are shown in figures 1 and 2 respectively for c_r, c_i versus θ and $\delta c_r/|\bar{\phi}_w|, \delta c_i/|\bar{\phi}_w|$ versus θ. These results are based on the direct numerical solution of (2), using (3) as the outer boundary condition, (6) and (7) as wall boundary conditions, with chosen specified values of α, R and $\bar{\phi}_w$. The condition $\bar{\phi}_d = 1$ is applied at $d = 2$. Also $\bar{\phi}_w = |\bar{\phi}_w| e^{i\theta}$ was specified as a complex parameter by using chosen values of $|\bar{\phi}_w|$ and θ for each run of (2). And, $\bar{\phi}'_w$ was taken as $\bar{\phi}'_w = -U'_w \bar{\phi}_w / c$ (see (7)). The point chosen is at $\alpha = 0.733, R = 2562.8$ (figures are not round since originally the normalization for y was done using the displacement thickness δ^*)

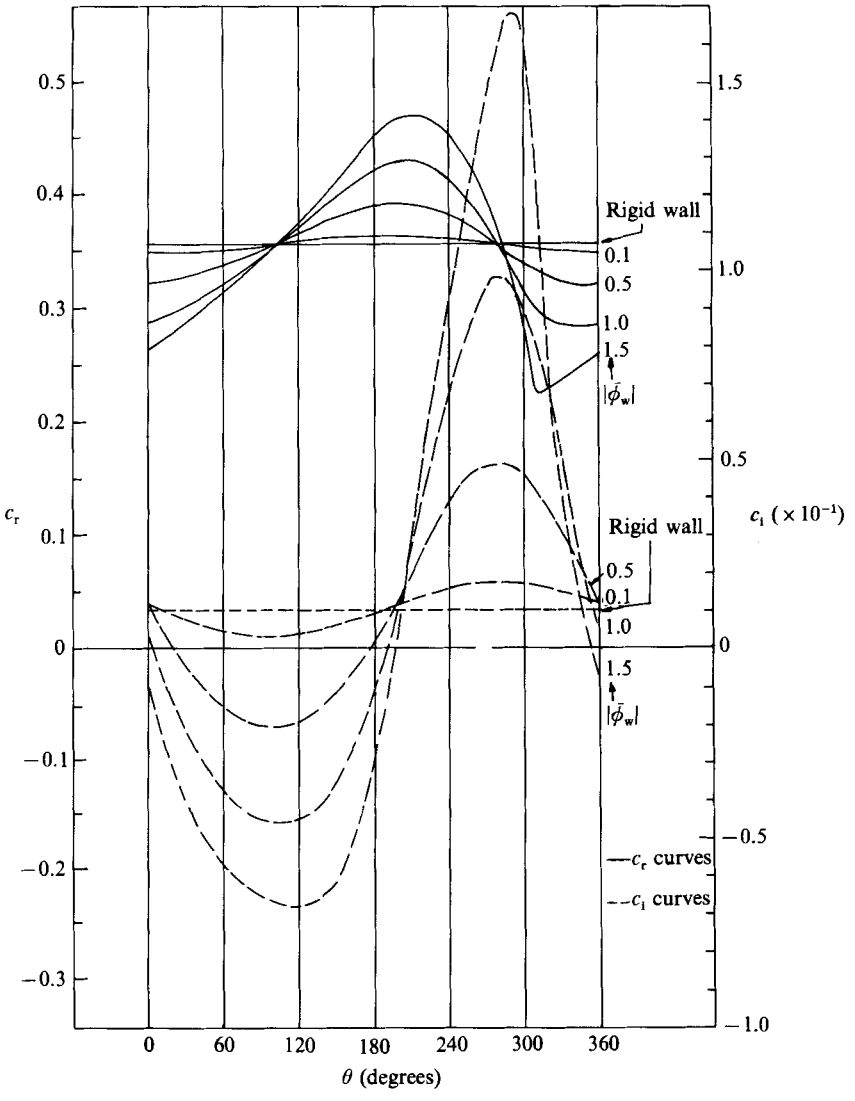

FIGURE 1. Curves for c_r (——), c_i (– – –) versus θ, for different $|\bar{\phi}_w|$, depicting TS mode class. All results in figures 1–21 are for $R = 2562.8$, $\alpha = 0.733$.

corresponding approximately to the point of maximum amplification within the rigid-wall neutral curve, at the given R. Figures 1 and 2 provide direct numerical proof to bear out amply the contentions regarding (31)–(34). Also, it is observed that when $|\bar{\phi}_w| = 1.5$ the sinusoidal character of the curves becomes distorted. As will be seen later, this distortion actually leads to bifurcation of modes at still higher values of $|\bar{\phi}_w|$, which amounts to a breakdown of the simple linearization postulated in (28). It is also seen from figures 1 and 2 that the value of θ_0, i.e. the phase angle of λ, is $\theta_0 \approx 0°$, although small changes in θ_0 do take place as $|\bar{\phi}_w|$ increases.

The significance of the above results is that two zero-crossings are observed to occur for c_i, one for $\theta \approx 0°$ and the other for $\theta \approx 180°$. Also there is a substantial region in $0° < \theta < 180°$ in which c_i is negative, and were it to be possible to remain in this region stabilization of the TS-type modes would actually be assured. *Prima*

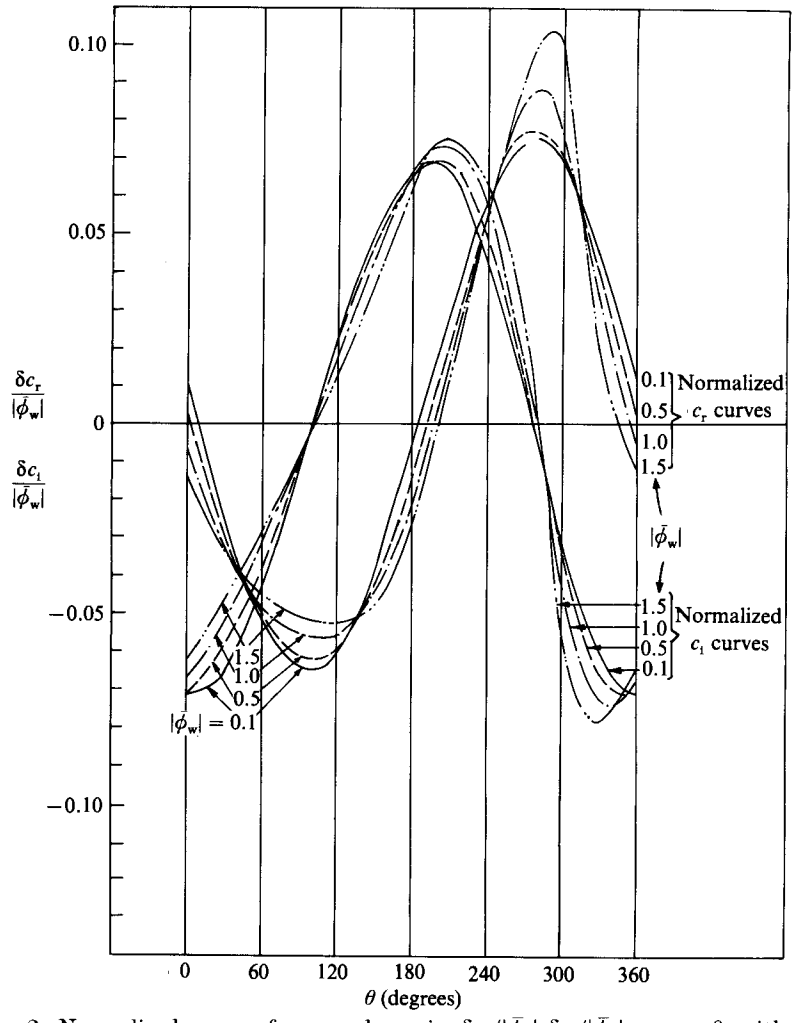

FIGURE 2. Normalized curves for c_r and c_i, viz. $\delta c_r/|\bar{\phi}_w|, \delta c_i/|\bar{\phi}_w|$ versus θ, with $c_r = \bar{c}_r + \delta c_r$ and $c_i = \bar{c}_i + \delta c_i$, where $\bar{c}_r, \bar{c}_i$ correspond to the rigid-wall eigenvalue. Results are for different values of $|\bar{\phi}_w|$ for the TS mode class.

facie this result is very significant, but this leads us to the question of physical realizability of modes, some aspects of which are discussed next.

The question of physical realizability of a proposed kinematic situation is in part connected with the admittance $Y\,(= Y_r + \mathrm{i}Y_i)$ defined in (12). For instance at a zero-crossing of c_i, if the sign of Y_r is negative then such a situation is not physically realizable as this would be tantamount to the existence of perpetual motion at least for passive surfaces. Whereas if at $c_i = 0, Y_r = 0$, then such a situation could be (though not always) physically realizable. This stipulation regarding physical realizability, in terms of the sign of Y_r, can be made strictly speaking only for $c_i = 0$, because it is only for $c_i = 0$ that a physical significance and meaning can be attached to the admittance Y. For regions where c_i is not zero, the sign of Y_r is usually not a good guide for physical realizability, except for the TS-type modes. However a method has been developed by which physical realizability can be ascertained in terms of equivalent material properties of the compliant surface, and this will be discussed in due course.

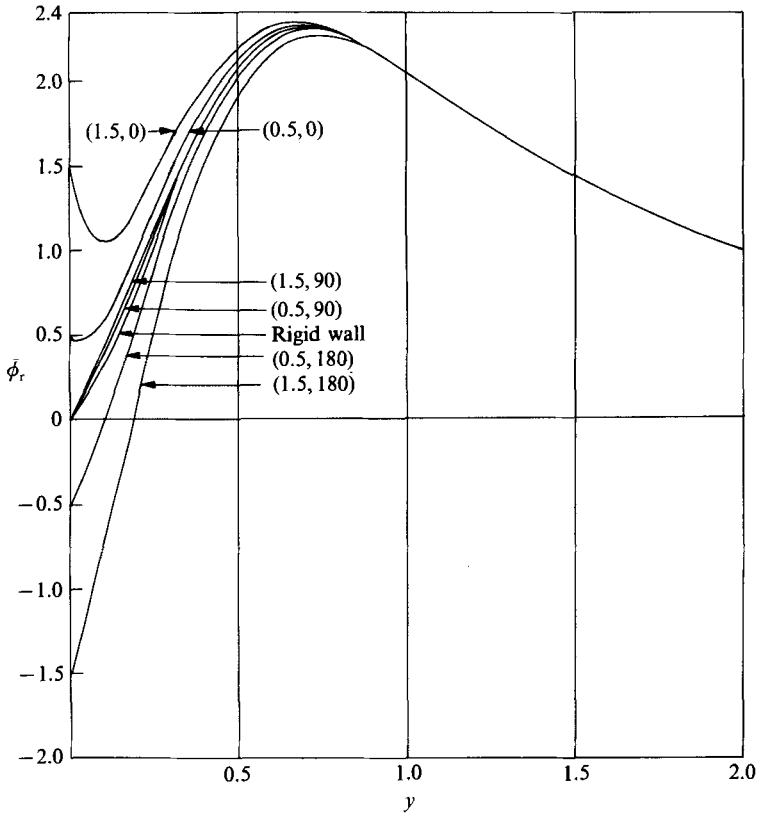

FIGURE 3. Curves for $\bar{\phi}_r$ versus y for a rigid wall and for the TS mode class. Figures in parentheses indicate $|\bar{\phi}_w|$ and θ (degrees) according to the format $(|\bar{\phi}_w|, \theta)$.

The above discussion on the importance of Y justifies examining its behaviour with changes in $|\bar{\phi}_w|$ and θ, as done for c. It is seen from (10)–(12) that Y depends on the distribution of $\bar{\phi}$. Benjamin (1959) has shown that for long waves the amplitude of the (fluctuating) pressure should remain approximately a real constant. We also note that if the effect of change in $\bar{\phi}_w$ and θ on the distribution of $\bar{\phi}$ is confined to within the boundary layer, then $\hat{p}_w$ will be more or less independent of variations in $|\bar{\phi}_w|$ and θ. We have found that this is in fact the case for TS-type modes. Figures 3 and 4 respectively show the plots for the real and imaginary parts of $\bar{\phi}$, i.e. $\bar{\phi}_r$ and $\bar{\phi}_i$, for different values of $|\bar{\phi}_w|$ and θ, including for the rigid-wall case for which $\bar{\phi}_w = 0$. The plots show that the change in the shape of $\bar{\phi}$, with the deviation of $\bar{\phi}_w$ from zero, is mainly confined to within the boundary layer. Moreover, with the normalization $\bar{\phi}_d = 1$, the integral $\int_0^\infty \bar{\phi}\,dy$ is predominantly real. From (11), this leads to two conclusions: first that $\hat{p}_w$ is approximately independent of changes in $\bar{\phi}_w$, and secondly that $\hat{p}_w$ is approximately a *real* constant for TS-type modes, at a given α and R. This confirms Benjamin's contention.

The behaviour of Y, consequent on the behaviour of $\hat{p}_w$ described above, is as follows. It is seen from (12) that Y should vary with $|\bar{\phi}_w|$ and θ in the following manner:

$$Y_r = -\frac{\alpha}{\hat{p}_w}|\bar{\phi}_w| \sin\theta, \quad \frac{Y_r}{|\bar{\phi}_w|} = -\frac{\alpha}{\hat{p}_w}\sin\theta, \tag{35a, b}$$

$$Y_i = \frac{\alpha}{\hat{p}_w}|\bar{\phi}_w| \cos\theta, \quad \frac{Y_i}{|\bar{\phi}_w|} = \frac{\alpha}{\hat{p}_w}\cos\theta, \tag{36a, b}$$

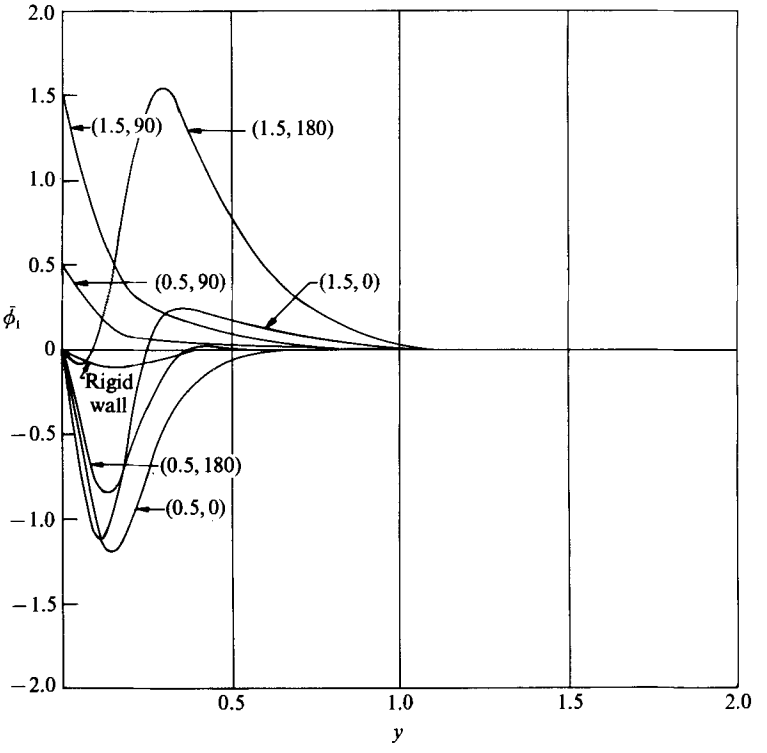

FIGURE 4. Curves for $\bar{\phi}_i$ versus y for a rigid wall and for the TS mode class. Figures in parentheses indicate $|\bar{\phi}_w|$ and θ (degrees) according to the format $(|\bar{\phi}_w|, \theta)$.

In the above equations, since $\hat{p}_w$ is approximately a real constant, the Y_r, Y_i versus θ curves are respectively negative sine and cosine curves. This is illustrated in figure 5 which shows the $Y_r/|\bar{\phi}_w|$, $Y_i/|\bar{\phi}_w|$ versus θ curves, for different values of $|\bar{\phi}_w|$. Again the results are based on direct numerical solution, and the curves amply bear out the contentions made regarding the behaviour of Y and $\hat{p}_w$. In particular, the approximate merging of the $Y_r/|\bar{\phi}_w|$, $Y_i/|\bar{\phi}_w|$ versus θ curves is very conclusive. Moreover, in figure 6 sample plots are shown for $\hat{p}_w$ versus θ, $\bar{a}$ versus θ, θ_{pa} versus θ, for $|\bar{\phi}_w| = 0.5$ with $\alpha = 0.733$ and $R = 2562.8$, where $\theta_{pa} = [\arg(\hat{p}_w) - \arg(\bar{a})]$ is the phase difference between the wall pressure and the wall displacement. In this figure $\hat{p}_w$ is shown to be approximately a real constant.

Upon reviewing figures 1, 2, 5 and 6 it transpires that δc_i and Y_r have almost the same phase, which is to say that generally speaking in the region $0° < \theta < 180°$, where c_i is negative, Y_r is also negative. *Prima facie* this is not a very encouraging situation so far as physical realizability of the $c_i < 0$ region is concerned, but as mentioned above, final conclusions regarding physical realizability should not be drawn based on the sign of Y_r alone, when $c_i \neq 0$.

Let us now concentrate our attention on the two regions $\theta \approx 0°$ and $\theta \approx 180°$ corresponding to the zero-crossings of the c_i versus θ curves. Amplified plots for the region $\theta \approx 180°$ are shown in figure 7. It is seen from this figure that the subtle change in phase difference between c_i and Y_r, caused as $|\bar{\phi}_w|$ increases, renders the point $c_i = 0$ physically realizable or otherwise. When $|\bar{\phi}_w| = 0.5$ then both at $\theta \approx 0°$ and at $\theta \approx 180°$, $Y_r < 0$ when $c_i = 0$. Therefore neither of these situations of neutral stability is physically realizable. Whereas when $|\bar{\phi}_w| = 1.5$, then both at $\theta \approx 0°$ and $\theta \approx 180°$,

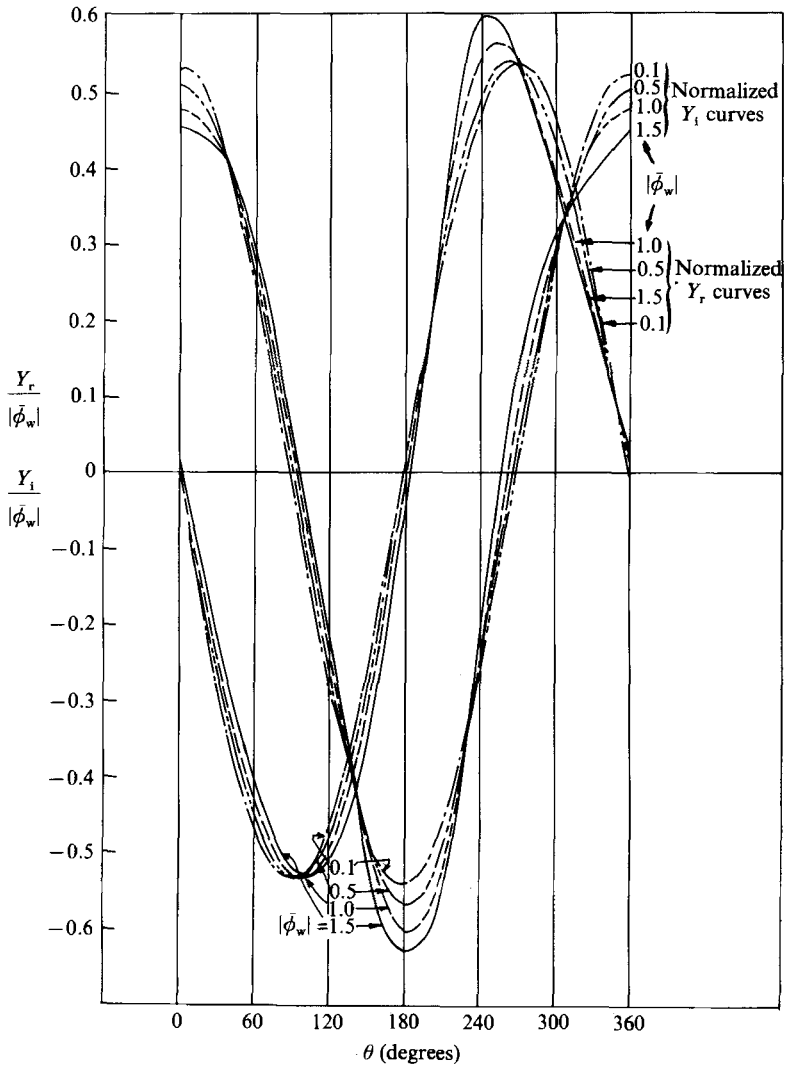

FIGURE 5. Normalized curves for Y_r and Y_i, viz. $Y_r/|\bar{\phi}_w|$, $Y_i/|\bar{\phi}_w|$ versus θ, for different values of $|\bar{\phi}_w|$ for the TS mode class.

$Y_r > 0$ when $c_i = 0$. These latter two situations of neutral stability therefore pass a crucial test for physical realizability. Yet the point $c_i = 0$, $|\bar{\phi}_w| = 1.5$, near $\theta = 0°$, is not physically realizable for another reason, because $Y_i > 0$ at this point, which is tantamount to an imaginary value for the surface wave speed c_0 (see (14)). Thus it is seen that the region of attention is $\theta \approx 180°$ where if $|\bar{\phi}_w|$ is sufficiently large then the state $c_i = 0$ may be physically realized. Incidentally the region $\theta \approx 180°$ also corresponds to Benjamin (1960) and Landahl's (1962) neutral curves for TS-type modes in the pliable-wall case. Benjamin for instance considers $A_i = 0$ with $A_r < 0$, corresponding to $Y_r = 0$ and $Y_i < 0$, for his neutral curve. Moreover, with reference to figure 7 ($c_i = 0, \theta \approx 180°$), it is seen that if one were to move from the point $c_i = 0$ in the direction of increasing Y_r, then $c_i > 0$ and increasing. This implies that if damping is increased in a neutral TS-type mode then this leads to destabilization, confirming this earlier important finding of Benjamin and Landahl. Figure 7 also

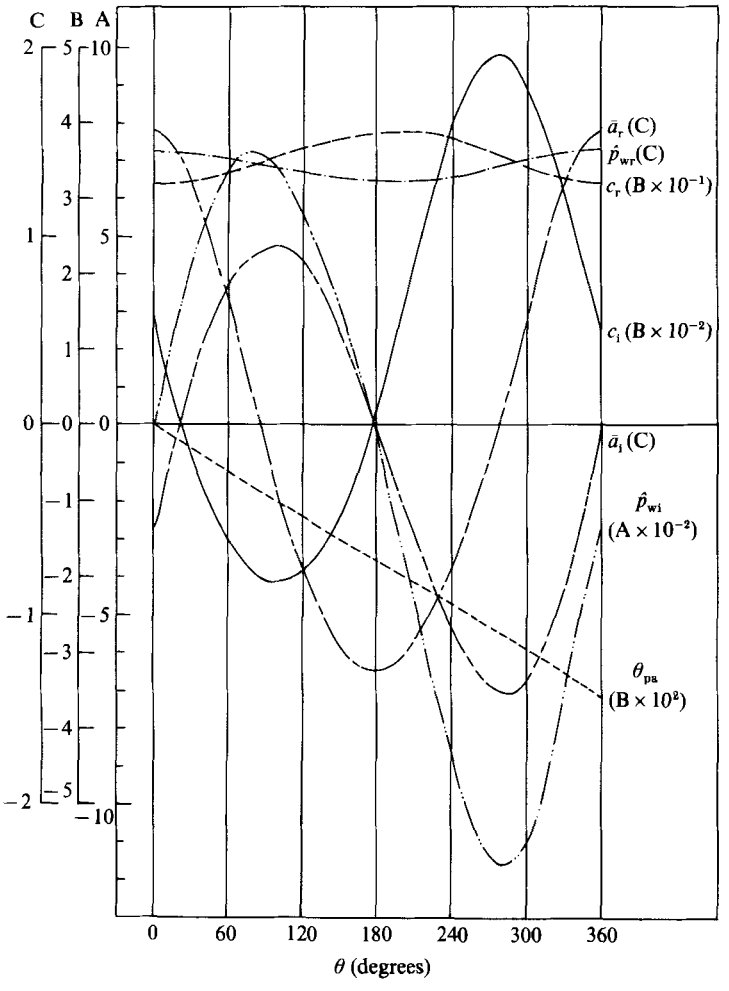

FIGURE 6. Curves for wall pressure ($\hat{p}_{wr}, \hat{p}_{wi}$), wall displacement ($\bar{a}_r, \bar{a}_i$), pressure-to-displacement phase difference $\theta_{pa}[= \arg(\hat{p}_w) - \arg(\bar{a})]$, c_r and c_i versus θ, with $|\bar{\phi}_w| = 0.5$. Results are for the TS mode class.

reveals the basic difficulty of stabilizing TS-type modes. The problem is that the vast region corresponding to $c_i < 0$ in $0° < \theta < 180°$ cannot be approached once the barrier $Y_r = 0$ is reached from the side $Y_r > 0$. Moreover, a possible realizable 'stable pocket' is confined only to the very small region in θ (see curve for $|\bar{\phi}_w| = 1.5$ near $\theta \approx 180°$ in figure 7) bounded by $c_i < 0$, $Y_r = 0$ and $c_i = 0$, $Y_r > 0$. From a practical standpoint it is a rather critical design problem to remain within such a 'stable-pocket' as this would require a rather exacting choice of material properties of the wall. Moreover, a choice of a set of material properties giving stability at a particular α and R does not guarantee that the TS-type modes will remain confined within 'stable-pockets' at other points in the (α, R)-plane. This is also the reason why a variety of pliable-wall neutral curves are obtained for the TS-type modes when either the model for the wall, or the material properties of the wall, are changed. Such neutral curves may be seen in the various different works starting from Landahl (1962) and up to Carpenter & Garrad (1985).

After investigating the TS-type modes at other representative points in the (α, R)-

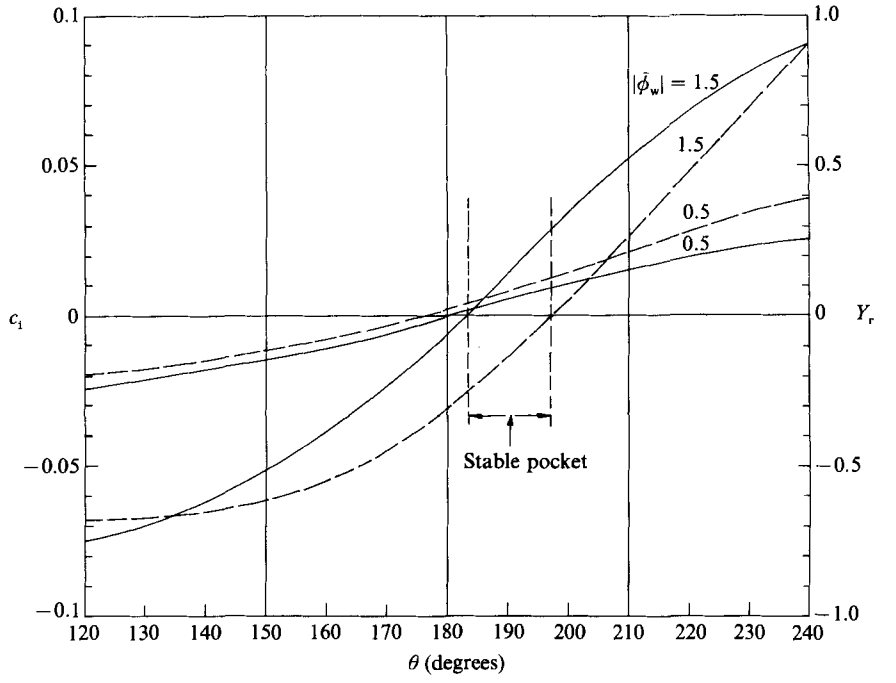

FIGURE 7. Curves for c_i (– – –) and Y_r (——) versus θ, with an enlarged scale for θ around $\theta = 180°$, for $|\bar{\phi}_w| = 0.5$, 1.5 and for the TS mode class. The figure shows the existence of a 'stable pocket' for $|\bar{\phi}_w| = 1.5$.

plane, it was found that the behaviour of these modes is essentially similar to that at the point at $\alpha = 0.733$, $R = 2562.8$, namely that 'stable pockets', when these do exist, are confined to a very narrow band of θ in the region $\theta \approx 180°$. In our opinion therefore, one ought not to try and 'stabilize' TS-type modes, because it would require a very exacting choice of wall material properties. Secondly, such properties would need to change with position in the (α, R)-plane to meet the exacting requirement of remaining within 'stable pockets'. As a design problem this seems to be virtually intractable. The best way to handle the situation, in our opinion, is to create conditions such that the TS modes just do not exist. How this may be achieved we shall discuss below.

5. The bifurcation of modes

We next have a look at the manner in which the TS-type modes bifurcate into other modes. It is also worth examining the distinct classes of modes that exist in the problem. We begin the study of bifurcation of modes by looking at figures 8 and 9 which give more exhaustive plots of c_r, c_i versus θ, at $\alpha = 0.733$, $R = 2562.8$. It is seen that as $|\bar{\phi}_w|$ is increased to about $|\bar{\phi}_w| = 2.0$, the familiar TS-type mode class undergoes a bifurcation. To avoid confusion we shall use 'mode' for a particular mode corresponding to one set of values of α, R, $|\bar{\phi}_w|$ and θ, and 'mode class' or 'class of modes' will be used to denote a group of modes that have certain identifiable common features. Thus with reference to figures 8 and 9 all TS-type modes for which the c_r, c_i versus θ curves form a closed loop in one cycle of 0–360° in θ, will be deemed as belonging to the TS-mode class. The c_r, c_i versus θ curves for $|\bar{\phi}_w| = 2.0$ close over

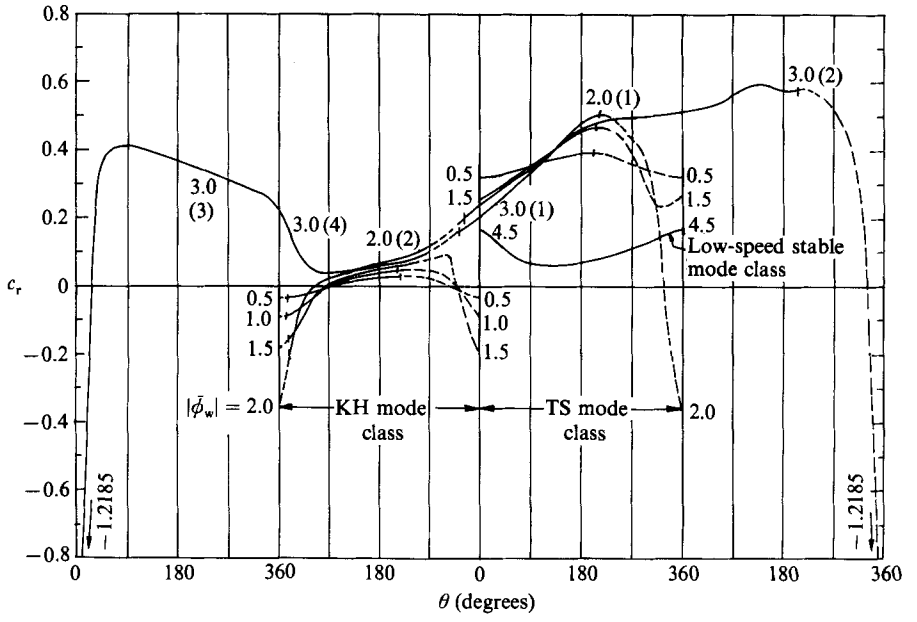

FIGURE 8. Curves for c_r versus θ for different $|\bar{\phi}_w|$, depicting different mode classes and bifurcation of mode classes. Figures shown on curves indicate value of $|\bar{\phi}_w|$, and figures in parentheses indicate order of multiplicity of the 0–360° cycle. Solid and broken lines respectively indicate stable and unstale regions.

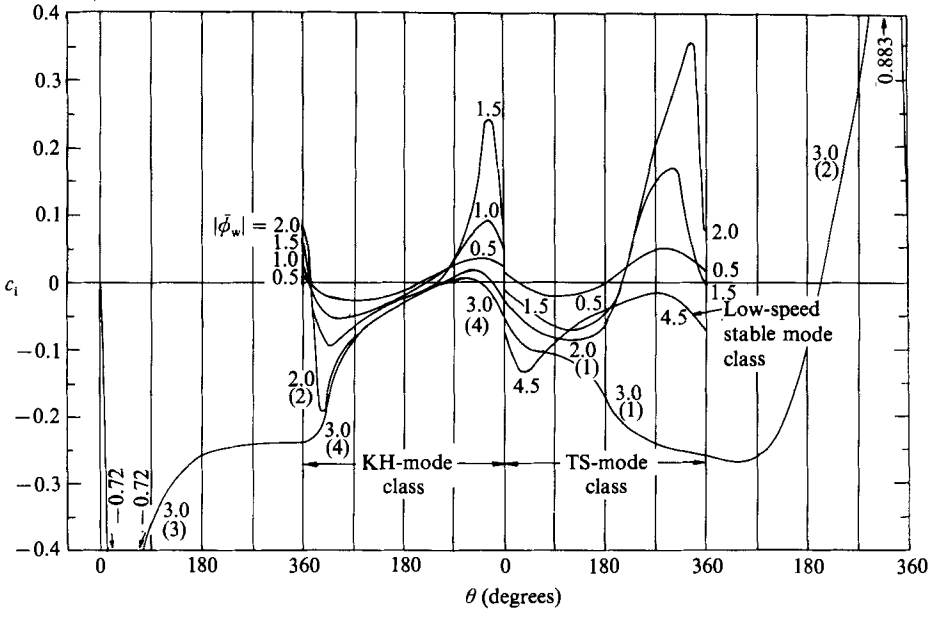

FIGURE 9. Curves for c_i versus θ for different $|\bar{\phi}_w|$, depicting different mode classes and bifurcation of mode classes. Figures shown on curves indicate value of $|\bar{\phi}_w|$, and figures in parentheses indicate order of multiplicity of the 0–360° cycle.

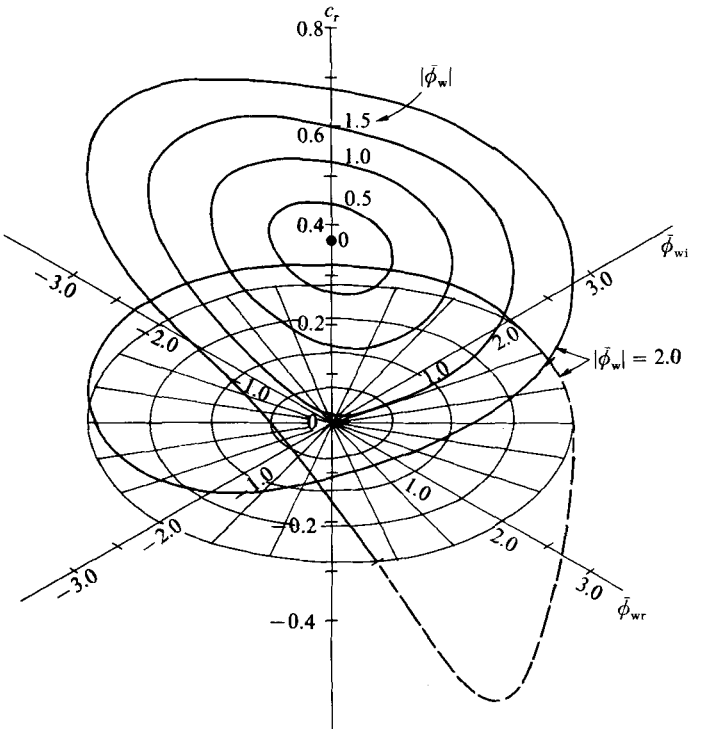

FIGURE 10. Isometric plots for c_r versus θ for different $|\bar{\phi}_w|$, depicting TS mode class and bifurcation from a TS mode class to a KH mode class for $|\bar{\phi}_w| = 2.0$. ——, $c_r > 0$; – – –, $c_r < 0$; ●, rigid wall with $c_r = 0.3564$.

two cycles in 0°–360°; so this mode class is transitional and belongs in one part to the TS-mode class and in the other part to some other mode class which we shall see later to be as the Kelvin–Helmholtz mode class. This bifurcation of mode classes is further illustrated in an isometric plot of c_r versus θ in figure 10.

It will be pertinent at this stage to examine how the concept of bifurcation is compatible with the theory outlined earlier in §2.2. It was mentioned earlier that a family of solutions for ϕ is characterized by $\phi = \phi(\bar{\phi}_w, c)$. Now at a given value of $|\bar{\phi}_w|$ and θ it is sometimes possible to find two or more values of the pliable-wall eigenvalue c^*, from (20). Thus if c_1^* and c_2^* be two such eigenvalues then $\phi = \phi(\bar{\phi}_w, c_1^*)$ and $\phi = \phi(\bar{\phi}_w, c_2^*)$ represent two distinct families of ϕ. Basically this is similar to the well-known situation for the rigid-wall case (for which $\bar{\phi}_w = 0$) where there is one principal eigenvalue for $c\,(= \bar{c})$, and also higher-order eigenvalues. Further, for the pliable-wall case, when two distinct eigenvalues c_1^* and c_2^* are obtained for a given $|\bar{\phi}_w|$ and θ, the corresponding $\bar{\phi}$-functions are completely different in shape although $\bar{\phi}_w$ is the same for both. Also the normalized wall displacements are different in the two cases, given respectively by $\bar{a}_1 = \bar{\phi}_w/c_1^*$ and $\bar{a}_2 = \bar{\phi}_w/c_2^*$. Figure 11 shows the shapes of $\bar{\phi}$ for $|\bar{\phi}_w| = 2.0$ and $\theta = 180°$ for the two distinct eigenvalues for c given respectively by $c = 0.4838 - i0.05568$ (TS-type) and $c = 0.052037 - i0.02936$ (KH-type).

The next two plots that attract attention in figures 8 and 9 are the c_r, c_i versus θ curves corresponding to $|\bar{\phi}_w| = 3.0$. It is seen that the respective curves for c_r and c_i close over four cycles of 0°–360°, which means that there are further bifurcations of mode classes, and the mode class corresponding to $|\bar{\phi}_w| = 3.0$ is also transitional.

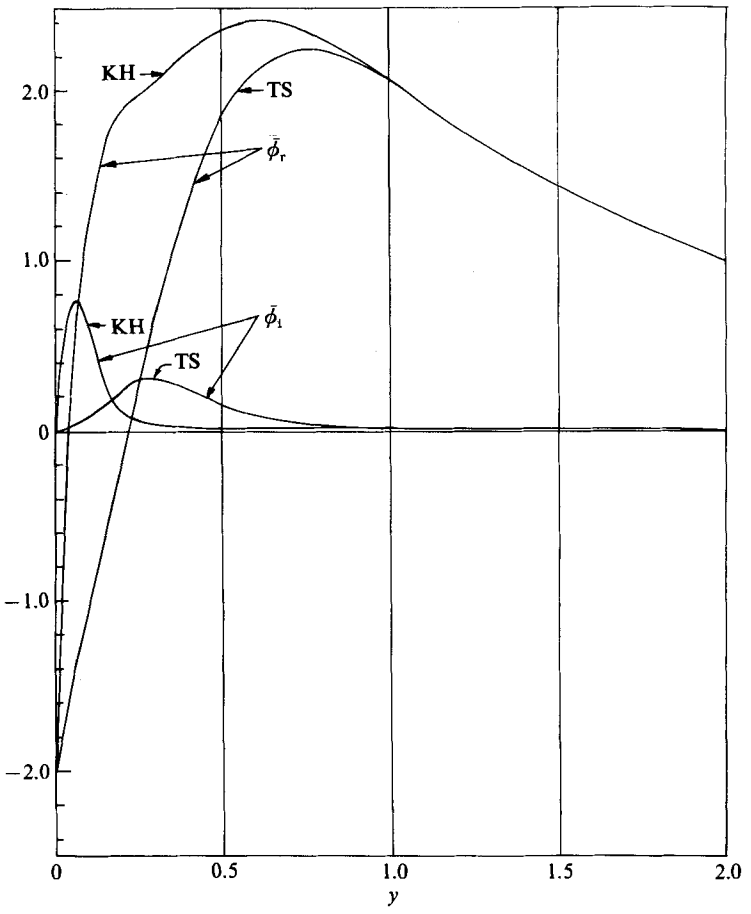

FIGURE 11. Curves for $\bar{\phi}$ versus y for TS and KH modes for $|\bar{\phi}_w| = 2.0$ and $\theta = 180°$. See bifurcation of mode classes for $|\bar{\phi}_w| = 2.0$, in figure 10.

It will be interesting therefore to identify and examine the regular mode classes, meaning thereby those mode classes that close within one cycle of 0°–360°. Three such mode classes are identified in figures 8 and 9, and others will be identified later. Apart from the TS mode class discussed in detail earlier, the two other mode classes shown in figures 8 and 9 are respectively called the Kelvin–Helmholtz (KH) mode class and the 'low-speed stable' mode class. The latter corresponds to low values of c_r and high values of $|\bar{\phi}_w|$, from about $|\bar{\phi}_w| = 4.5$ and above. This mode class is very stable although it belongs to high values of $|\bar{\phi}_w|$, and as such it is not of much interest here.

The KH mode class, which will be discussed in detail later, is interesting and important. It appears that the TS and the KH mode classes are the only two mode classes that exist for low-values of $|\bar{\phi}_w|$ and even in the limit $|\bar{\phi}_w| \to 0$. Yet these two mode classes are completely and totally distinct despite a common intersection of values of $|\bar{\phi}_w|$ and θ.

Another very important mode class is the resonant (R) mode class. The terms Kelvin–Helmholtz mode class and resonant mode class follow from Benjamin's (1960) nomenclature; the reasons for attributing these names to the different mode classes in the present work will be discussed below. Bifurcation to the R mode class

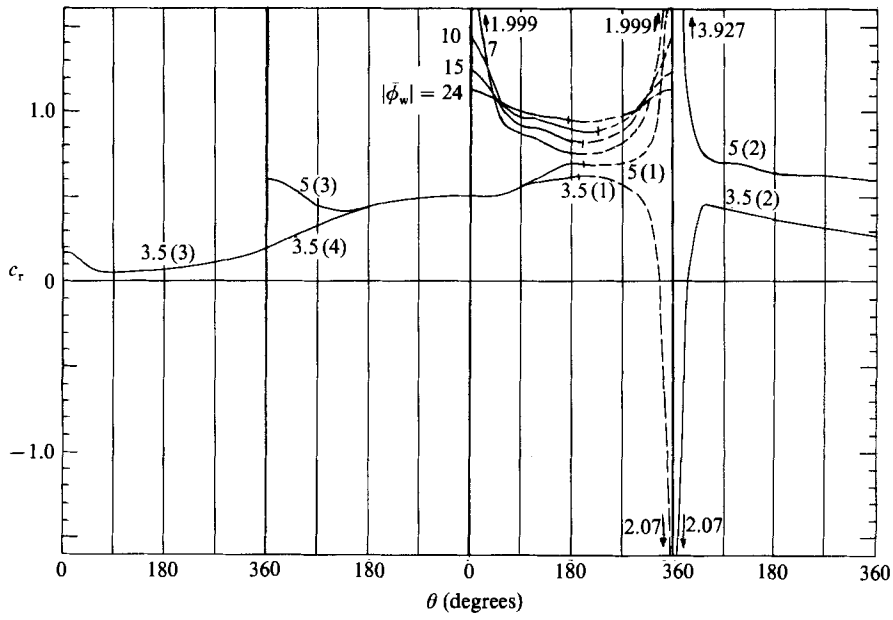

FIGURE 12. Curves for c_r versus θ for different $|\bar{\phi}_w|$, depicting the R mode class and bifurcation to transitional mode classes as the value of $|\bar{\phi}_w|$ is lowered. The latter phenomenon independently confirms the existence of 'modal coalescence' as reported by Carpenter & Garrad (1985, 1986). Figures shown on curves indicate value of $|\bar{\phi}_w|$, and figures in parentheses indicate order of multiplicity of the 0–360° cycle. Solid and broken lines respectively indicate stable and unstable regions.

is shown in figures 12 and 13, respectively for the c_r, c_i versus θ curves. The figures are more or less self-explanatory. However, there is one important point to note. The graphs corresponding respectively to $|\bar{\phi}_w| = 3.5$ and $|\bar{\phi}_w| = 5.0$, both belonging to different transitional mode classes, reveal an interesting feature. It appears that c_r develops a singularity going from $-\infty$ to $+\infty$ across these two transitional mode classes at a point near $\theta = 360°$. However, $c_i \to +\infty$ for both limbs of the singularity for c_r. This singularity has great significance in the matter of designing stabilizing coatings, and we believe that the concept of 'modal-coalescence' introduced by Carpenter & Garrad (1985) is related to the behaviour of modes near this singularity. Besides, the singularity itself may be related to static divergence.

It appears from figures 12 and 13 that the regular R mode class exists only for high values of $|\bar{\phi}_w|$. Secondly, these modes are high-speed modes, that is c_r for these modes is mainly in the range $c_r \geqslant 0.7$. Further, it appears that the TS-to-R bifurcation, although occurring through transitional mode classes like $|\bar{\phi}_w| = 3.5$ and $|\bar{\phi}_w| = 5.0$, is discontinuous in the sense that the bifurcation occurs via a singularity. Also the two transitional mode classes, viz. for $|\bar{\phi}_w| = 3.5$ and $|\bar{\phi}_w| = 5.0$, are very important in regard to flow stabilization because both these mode classes have a large unstable region as shown in figures 12 and 13.

The manner in which the R mode class begins to distort and subsequently bifurcate into a transitional mode class, as the value of $|\bar{\phi}_w|$ is lowered, is illustrated in the plots of c_r versus θ in figure 12.

It is pertinent to mention that there is also a high-speed stable mode class having high values of $|\bar{\phi}_w|$ and c_r similar to the R mode class. Since this mode class is entirely stable it is not of much interest here and is thus not shown in the figures.

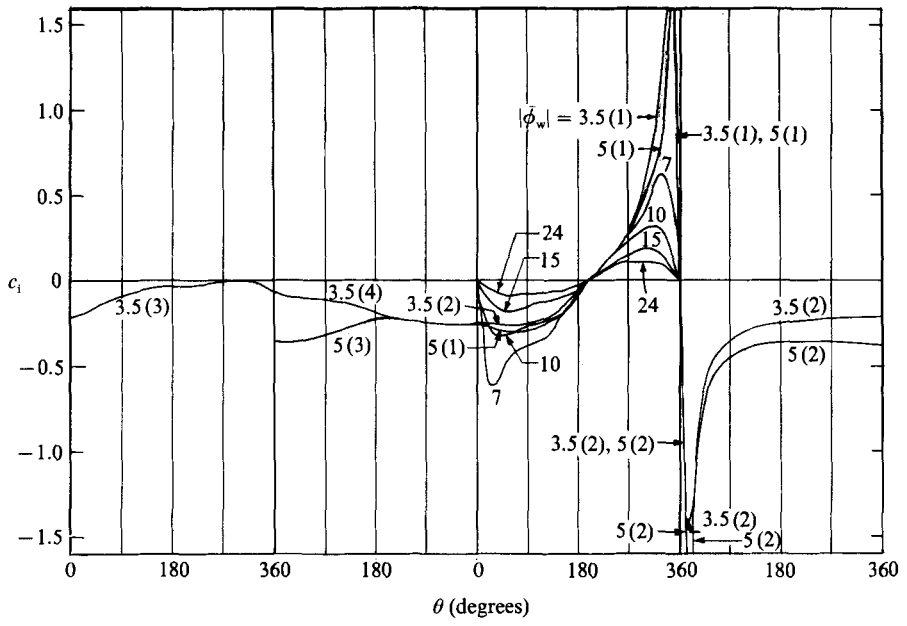

FIGURE 13. Curves for c_i versus θ for different $|\bar{\phi}_w|$, depicting the R mode class and bifurcation to transitional mode classes as the value of $|\bar{\phi}_w|$ is lowered. Figures shown on curves indicate value of $|\bar{\phi}_w|$, and figures in parentheses indicate order of multiplicity of the 0–360° cycle.

In summary, therefore, we may say that there are three regular mode classes that are of interest here, namely the TS, KH and R mode classes, and the nomenclature follows Benjamin's (1960) terminology. The Landahl (1962)–Benjamin (1963) classification based on energy methods will be discussed later. However, Benjamin's 'modes' represent only a very small subset of the totality of possibilities depicted by the 'mode classes'. Further there are also transitional mode classes mainly in the region $|\bar{\phi}_w| = 2.0$ to $|\bar{\phi}_w| = 6.0$ which depict the regions of bifurcations of the regular mode classes. These transitional mode classes also depict large regions in θ where these are unstable, and, over part cycles of 0°–360° in θ, these mode classes depict behaviour corresponding to regular mode classes. For instance, the relatively low c_r (≈ 0.5) resonant mode, conceived by Benjamin and Landahl, does not belong to the regular resonant mode class, but to a transitional mode class.

All results discussed so far pertain to one point in the (α, R)-plane, that at $\alpha = 0.733$ and $R = 2562.8$. A few other representative points were also investigated in detail, although plots for these are not given herein, including one at a low (subcritical) value of $R = 200$ with $\alpha = 0.4$, at a low value of $\alpha = 0.03$ with $R = 2500$, one above the neutral curve at $\alpha = 1.25$ and $R = 2500$, and one below the neutral curve at $\alpha = 0.4$ and $R = 2500$. All these points show a qualitative similarity to the point at $\alpha = 0.733$ and $R = 2562.8$, in respect of behaviour of regular mode classes and in respect of bifurcation of modes. However, as is to be expected, the ranges of values of $|\bar{\phi}_w|$ over which the regular mode classes exist, and the threshold values of $|\bar{\phi}_w|$ for bifurcation from regular mode classes to transitional mode classes to occur, are different at different points in the (α, R)-plane. An exhaustive study of all points in the (α, R)-plane would be prohibitively elaborate although not impossible. In the rigid-wall problem it is only necessary to investigate one mode at each point in the (α, R)-plane, whereas in the pliable-wall problem entire classes of modes have to be

investigated at each point. Actually such an exhaustive study is unnecessary, especially because the basic qualitative behaviour is similar everywhere. Rather, if the aim is to design a suitable stabilizing coating then one has to look for two things from the results of the kinematic model: the most viable stable region that is also physically realizable; and, in such a viable stable region, the particular mechanism that could potentially become most dangerous in causing destabilization. These questions will be discussed in §8, but before that we look at the behaviour of the KH mode class and the R mode class in some detail.

6. The Kelvin–Helmholtz mode class

It was mentioned earlier that the KH mode class exists for low values of $|\bar{\phi}_w|$, and the limit $|\bar{\phi}_w| \to 0$ does not correspond to the rigid-wall limit in this case. To understand this we look at (7) and (18). We note from (18) that the limit $|\bar{\phi}_w| \to 0$ is reached for a non-zero value of $\bar{a}$ if $|c| \to 0$, in which case it is seen from (7) that when $|\bar{\phi}_w| \to 0$, $\bar{\phi}'_w \neq 0$ and $\bar{\phi}'_w$ is given as $\bar{\phi}'_w = -\bar{a}_0 U'_w$, where $\bar{a}_0$ is the limiting value of $\bar{a}$. It is seen therefore, that the KH mode class is quite distinct from the TS mode class.

The nomenclature 'Kelvin–Helmholtz' mode class now begins to be understood. In the limit $|\bar{\phi}_w| \to 0$ with $|c| \to 0$ this mode represents a stationary periodic ripple with spatial wavenumber α and amplitude $\bar{a}_0$, and since $|c| \to 0$ this mode is neutrally stable in the limit. This is in fact what the neutrally stable classical Kelvin–Helmholtz mode is. Further evidence is provided from a figure† similar to figure 6 where $\hat{p}_w$, c, $\bar{a}$ and θ_{pa} are plotted versus θ for $|\bar{\phi}_w| = 0.1$ for the KH-mode class. This figure shows that θ_{pa}, which is the phase difference between $\hat{p}_w$ and $\bar{a}$, is nearly constant at 180° over the entire range of θ. As expected, $\hat{p}_w$ and $\bar{a}$ are in antiphase for KH type modes. It must however be emphasized that the present classification does not readily adapt to Landahl (1962) and Benjamin's (1963) classification based on energy analysis. By energy analysis, what have been called Kelvin–Helmholtz modes by Benjamin and Landahl probably belong to a small segment (i.e. a small range of values in θ) within one of the transitional mode classes herein. And, what has been called the KH mode class herein, possibly contains small segments in θ, the modes corresponding to which may be identified with what has been called static divergence, or, low-speed travelling wave flutter by Carpenter & Garrad (1986). It must be realized that classification of 'modes' as done by earlier workers, and classification of 'mode classes' as in the present work, could represent two different endeavours, since the former is a very small subset of the latter. Moreover to seek a connection between the two by energy analysis is not straightforward because there is no model *a priori* for the solid phase in the present analysis. We therefore depend on Benjamin's (1960) scheme of classification and nomenclature, and on other basic considerations, for assigning the name 'Kelvin–Helmholtz' mode class for this particular mode class described herein.

We next see whether or not certain predictions can be made for the KH-mode class, based on the formal solution (20), similarly as done for the TS-mode class. We use (20) with the caution that the fundamental solutions ϕ_1, ϕ_2 and ϕ_3 are not necessarily of the same form as in the classical Tollmien–Schlichting problem, especially when the critical layer becomes submerged in the wall viscous layer. However, ϕ_1 and ϕ_2 still imply the inviscid solutions and ϕ_3 the relevant viscous

† This, and other figures similarly discussed but not printed, are available from the authors or the Editor.

solution. Using $\bar{a}U'_w$ in place of $U'_w\bar{\phi}_w/c$ in (20), expanding and proceeding to the limit $|\bar{\phi}_w| \to 0$ we obtain the limiting value of $\bar{a}_0$ as

$$\bar{a}_0 = -\frac{1}{U'_w}\left[\frac{\Delta}{\phi_{3w}\Delta_1}\right]_0, \tag{37}$$

where subscript zero refers to the limiting state, and Δ and Δ_1 are given by (26) and (27) respectively. We also note that $\bar{a}, \bar{a}_0$ may be formally expressed as

$$\bar{a}_0 = \left.\frac{\partial\bar{\phi}_w}{\partial c}\right|_0, \tag{38}$$

$$\bar{a} = \bar{a}_0 + \left.\frac{\partial\bar{a}}{\partial c}\right|_0 \delta c + \ldots, \tag{39a}$$

$$= \left.\frac{\partial\bar{\phi}_w}{\partial c}\right|_0 + \left.\frac{\partial^2\bar{\phi}_w}{\partial c}\right|_0 \delta c + \ldots, \tag{39b}$$

where $c = c_0 + \delta c$. Also δc is meant to imply the departure from the limiting value c_0, and we know that $c_0 = 0$. We now expand (20) again, using (37) and remembering that $\bar{\phi}_w \sim O(\delta c)$. This gives

$$B_0\,\delta c + \bar{\phi}_w[\phi'_w\Delta_1]_0 = 0, \tag{40}$$

where

$$B_0 = \left[\frac{\partial\Delta}{\partial c} - \frac{\Delta}{\phi_{3w}\Delta_1}\frac{\partial(\phi_{3w}\Delta_1)}{\partial c} + U'_w\phi_{3w}\Delta_1\frac{\partial\bar{a}}{\partial c}\right]_0, \tag{41}$$

and the expressions in parenthesis subscripted by zero are evaluated at the limit $|c| \to 0$.

As in the TS case, δc may now be expressed in terms of a complex constant $\lambda_1 = |\lambda_1|\,e^{i\theta_1}$, from (40) and (41), as follows:

$$\delta c = -|\lambda_1|\,|\bar{\phi}_w|\,e^{i(\theta+\theta_1)}, \tag{42}$$

with

$$\lambda_1 = |\lambda_1|\,e^{i\theta_1} = \frac{B_0}{[\phi'_{3w}\Delta_1]_0}. \tag{43}$$

Thus the behaviour of δc_r and δc_i is again sinusoidal, and expressions for δc_r, δc_i, $\delta c_r/|\bar{\phi}_w|$ and $\delta c_i/|\bar{\phi}_w|$ are respectively the same as (31), (32), (33) and (34) with λ replaced by λ_1 and θ_0 replaced by θ_1. Two figures, similar to figure 2, were made showing normalized plots for $c_r/|\bar{\phi}_w|, c_i/|\bar{\phi}_w|$ (remembering $\delta c = c$, since $c_0 = 0$) versus θ, at $\alpha = 0.733, R = 2562.8$, for different values of $|\bar{\phi}_w|$. The first figure was for comparatively low values of $|\bar{\phi}_w|$ ($\leqslant 0.1$) and the scaling was near perfect. The second figure was for larger values of $|\bar{\phi}_w|$ (> 0.1) and the distortion of the sinusoidal character (leading to bifurcation of modes at higher values of $|\bar{\phi}_w|$) was apparent in this figure. Also from the first figure the value for θ_1, that is the phase of λ_1, was found to be $\theta_1 \approx -30°$.

Regarding the admittance Y, it should be mentioned in advance that the sign of Y_r is not a good guide to physical realizability of KH modes when $c_i \neq 0$, except when $c_i = 0$ exactly. Nevertheless, the scaling for Y is again given by (35*a*, *b*) and (36*a*, *b*), that is the same as for the TS-mode class, and for the same reasons as for the TS-mode class. In support, figures similar to figures 3 and 4 were plotted for the real and imaginary parts of the various $\bar{\phi}$-functions for the KH mode class with different

values of $|\bar{\phi}_w|$ and θ. In these figures also it could be seen that the effect of $|\bar{\phi}_w|$ on the distribution of $\bar{\phi}$ was confined to within the boundary layer. The shape of the $\bar{\phi}$-functions for the KH modes may be seen in figure 11 and the shape is quite distinct from that for the TS modes. Moreover, it has been contended earlier that $\hat{p}_w$ is approximately a real constant. Thus plots similar to figure 5 were made for $Y_r/|\bar{\phi}_w|$, $Y_i/|\bar{\phi}_w|$ versus θ, for different values of $|\bar{\phi}_w|$, and again these plots were found to merge as closely as they do in figure 5 and to have the same shape.

Since the physical realizability of KH modes cannot be satisfactorily ascertained on the basis of the sign of Y_r when $c_i \neq 0$, this aspect will be taken up later.

7. The resonant mode class

We now look at certain features of the R mode class. It has been mentioned earlier that this mode is characterized by high values of $|\bar{\phi}_w|$ and $c_r (\to 1)$. That this is the 'panel-flutter' mode can be seen from a figure similar to figure 6 where $\hat{p}_w$, c, $\bar{a}$ and θ_{pa} were plotted versus θ. This showed that $\hat{p}_w$ is neither predominantly real nor approximately a constant. However, θ_{pa} is approximately constant at 180° over the entire range of θ, as typically expected in panel flutter. Reference to figure 6 shows that θ_{pa} varies continuously with θ for the TS modes, whereas for KH and R modes θ_{pa} is approximately constant at 180°. This latter reason lends further justification in classifying KH and R modes as flow-induced surface instabilities FISI as Carpenter & Garrad (1985, 1986) have done.

The reason for the difference in behaviour of $\hat{p}_w$ in the R mode class, compared to the TS- and KH-mode classes, is understood from figure 14. Here, the real and imaginary parts of the $\bar{\phi}$-functions (for $|\bar{\phi}_w| = 24$ with different values of θ) are plotted for the R modes. It is seen that the shapes of $\bar{\phi}$ are strongly dependent on $|\bar{\phi}_w|$ and θ in the main range of y, quite in contrast to the other two mode classes. This is mainly because the value of $|\bar{\phi}_w|$ is large. Therefore, as may be inferred from (11), $\bar{p}_w$ cannot be expected to be a constant. Also it may be inferred from (12) that although the admittance Y will remain bounded in the limit $|\bar{\phi}_w| \to \infty$, Y will not show any sinusoidal behaviour with θ. This is also seen from (35*a*, *b*) and (36*a*, *b*) in which, unless $\hat{p}_w$ is approximately a constant, no sinusoidal behaviour may be expected of Y. Plots of Y_r, Y_i versus θ are therefore not given for the R modes at this stage.

It may be mentioned here that the physical realizability of R modes cannot be ascertained satisfactorily on the basis of the sign of Y_r for $c_i \neq 0$, except when $c_i = 0$ exactly. Thus, irregular variation of Y_r, Y_i with θ is not of much consequence at this stage, and the question of physical realizability of R modes is also deferred until the next section.

An approximate theory may still be postulated for the behaviour of c_r, c_i with θ for the R mode class, based on the formal solution (20). We assume that the limiting behaviour of the R mode class is given by $|\bar{\phi}_w| \to \infty$, and that the disturbances are neutrally stable in the limiting state. Further, $|\bar{\phi}_w| \to \infty$ is compatible only when the critical point moves to infinity, in which case the limiting value of c is given as $c_R = 1 + i0$. Henceforth subscript R will be used to depict this limiting state. Also, in using the formal solution (20), care must be taken to remember, as in the KH case earlier, that the forms of the fundamental solutions ϕ_1, ϕ_2, ϕ_3 are not the same as in the Tollmien–Schlichting problem. Nevertheless, ϕ_1 and ϕ_2 still typify the two inviscid solutions and ϕ_3 the viscous solution.

As before, the deviation from the limiting state is given by δc, with $c = c_R + \delta c$.

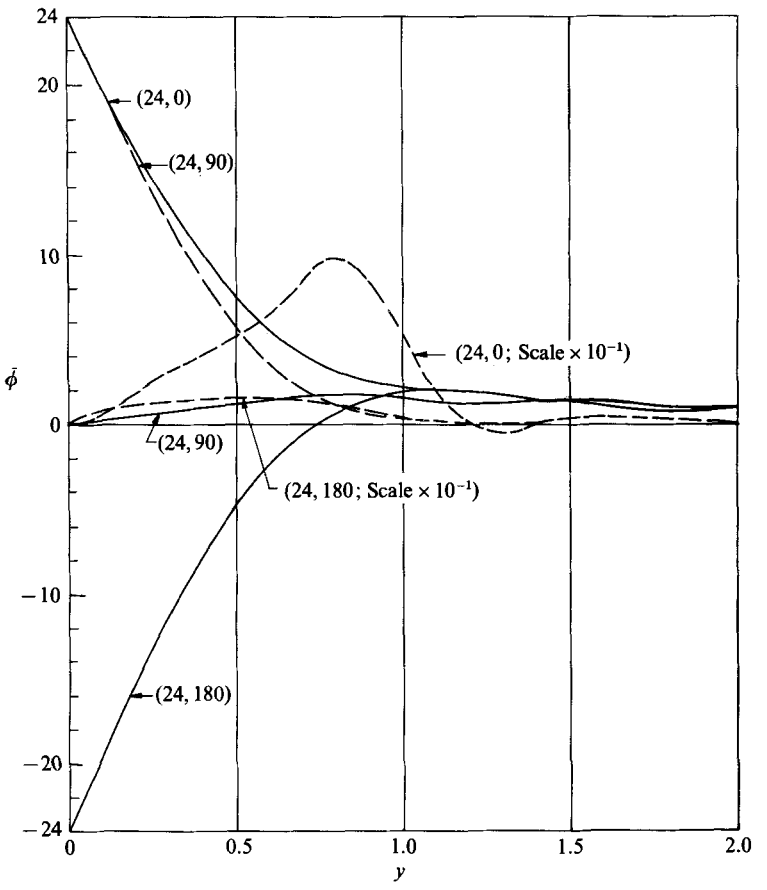

FIGURE 14. Curves for $\bar{\phi}$ versus y for the R mode class. Figures in parentheses indicate $|\bar{\phi}_w|$ and θ (degrees) according to the format $(|\bar{\phi}_w|, \theta)$. ——, $\bar{\phi}_r$; – – –, $\bar{\phi}_i$.

Also $1/|\bar{\phi}_w| \sim O(\delta c)$ since for $|\bar{\phi}_w| \to \infty, \delta c \to 0$. Upon expanding (20) and going to the limit one obtains the limiting value of c_R as

$$c_R = -U'_w \left[\frac{\phi_{3w}}{\phi'_{3w}}\right]_R. \tag{44}$$

It can be seen from (44) that although the limiting value exists, we cannot prove that $c_R = 1$, and this continues to be a heuristic assumption. However Carpenter & Garrad (1986) have proved this result. Thereafter, upon expanding (20), substituting (44) and retaining terms up to $O(\delta c)$, one obtains, as before, that

$$\delta c = \frac{\lambda_2}{|\bar{\phi}_w|} e^{-i\theta}, \tag{45}$$

where λ_2 is a complex constant defined as

$$\lambda_2 = |\lambda_2| e^{i\theta_2} = \left[\frac{\Delta}{\frac{\partial(\phi'_{3w}\Delta_1)}{\partial c} - \frac{U'_w \phi_{3w}\Delta_1}{c^2} + \frac{U'_w}{c}\frac{\partial(\phi_{3w}\Delta_1)}{\partial c}}\right]_R, \tag{46}$$

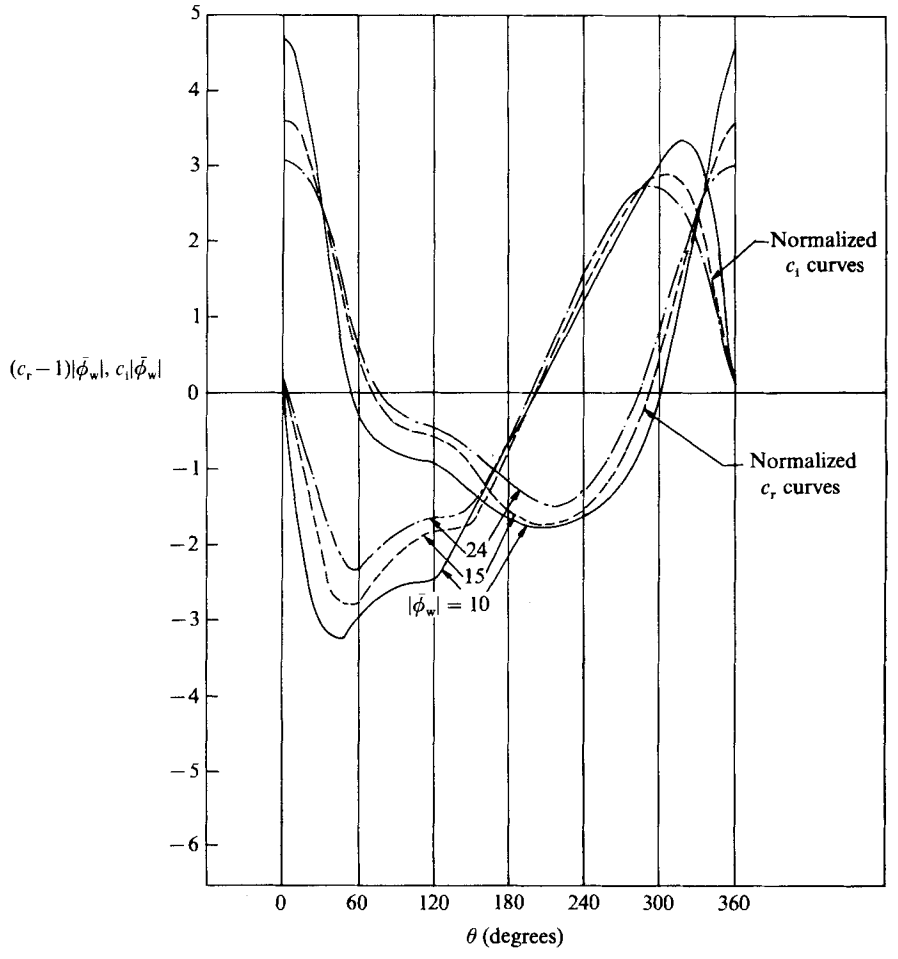

FIGURE 15. Normalized curves for c_r and c_i, viz. $(c_r-1)|\bar{\phi}_w|, c_i|\bar{\phi}_w|$, versus θ for different values of $|\bar{\phi}_w|$. Results are for the R mode class.

where Δ and Δ_1 are respectively given by (26) and (27), and the expression in square brackets in (46) is evaluated at the limit $c = c_R$.

The expressions for δc_r and δc_i are now given as below

$$\delta c_r = \frac{|\lambda_2|}{|\bar{\phi}_w|}\cos(\theta-\theta_2), \tag{47}$$

$$\delta c_i = -\frac{|\lambda_2|}{|\bar{\phi}_w|}\sin(\theta-\theta_2), \tag{48}$$

Thus it is seen from (47) and (48) that δc_r and δc_i again depict sinusoidal behaviour with θ, although this time they scale with $1/|\bar{\phi}_w|$, instead of $|\bar{\phi}_w|$ as earlier in the TS and KH mode classes. Plots of $\delta c_r|\bar{\phi}_w|, \delta c_i|\bar{\phi}_w|$ versus θ are given in figure 15, where $\delta c_r = c_r - 1$ and $\delta c_i = c_i$ (since $c_R = 1 + i0$). From the figure there is some approximate confirmation of the simple theory outlined earlier. Also the phase θ_2 of λ_2 is given as $\theta_2 \approx 0°$.

We conclude this section with the general remark that for both the KH and R mode classes $\delta c_i = c_i$. Therefore sinusoidal behaviour of c_i (i.e. δc_i) with θ implies that

in approximately one half of the cycle 0°–360° of θ, c_i is negative. Moreover, for the TS mode class also, there is a wide range of θ in which c_i is negative. It is therefore logical to try and ascertain the physical realizability of the $c_i < 0$ region. This is discussed next.

8. The physical realizability of modes

The question of physical realizability of modes, particularly those in the stable regions predicted by the kinematic model, has been mentioned earlier. It was pointed out that, except when $c_i = 0$ exactly, the sign of Y_r is not a sufficiently reliable index for ascertaining physical realizability, particularly for the KH and R modes. We evolve here a generalized procedure for ascertaining physical realizability by looking at the second expression for admittance Y_0, based on the solid side, as given by (14). This expression for Y_0 is based on the Benjamin–Landahl model for a stretched membrane. However, as in earlier discussions, we shall consider that the parameters c_0 and d in (14) are sufficiently generalized, and represent the *local equivalent* values for any complex model proposed for the backing compliant layer, at every set of operational conditions. Thereafter the limits that will be set on physical realizability are that neither c_0^2 nor d should be negative. The equivalent c_0^2 cannot be negative because that would amount to the compliant surface having negative resilience even to the static loading of the upper fluid. The equivalent d cannot be negative because a passive surface cannot irreversibly transfer energy to the upper fluid. It could be speculated however that a dolphin might, by activating its muscles and regulating its blood flow, be able to actively interact with the surrounding fluid and thus simulate 'negative damping'. Were it not for the fact that 'negative damping' could create conditions that would inhibit instabilities, as we shall see subsequently, it would probably not be worth speculating on such a possibility. However, for present purposes we will stipulate that the equivalent d cannot be negative in passive surfaces.

The procedure hereafter is to calculate c_0 and d for chosen values of m, from the results for the admittance Y based on the kinematic model. Remembering that $Y = Y_0$, we look at the separate equations for Y_r and Y_i based on (14):

$$Y_r = \frac{\left[c_i(c_0^2 + c_r^2 + c_i^2) + (c_r^2 + c_i^2)\frac{d}{\alpha}\right]}{D}, \tag{49}$$

$$Y_i = \frac{c_r(c_r^2 + c_i^2 - c_0^2)}{D}, \tag{50}$$

where

$$D = m\alpha\left[\left(c_0^2 - c_r^2 + c_i^2 + \frac{c_i d}{\alpha}\right)^2 + c_r^2\left(2c_i + \frac{d}{\alpha}\right)^2\right]. \tag{51}$$

Five representative points in the (α, R)-plane, referred to earlier, were investigated. These are at (0.733, 2562.8), (1.25, 2500), (0.4, 2500), (0.03, 2500) and (0.4, 200). Of these, detailed results and plots for the first point, at $\alpha = 0.733$ and $R = 2562.8$, are given herein. The results at the other points are generally similar, and any significant differences will be discussed here. The values of m chosen were 1, 1.5 and 2. No major qualitative changes were observed for the values of m in this range. Therefore results based on $m = 2$ are reported here for easy comparison with Landahl's (1962) results. Further, following Landahl, for $\alpha < 0.5$, m was modified to $m = 0.5/\alpha^2$ to avoid

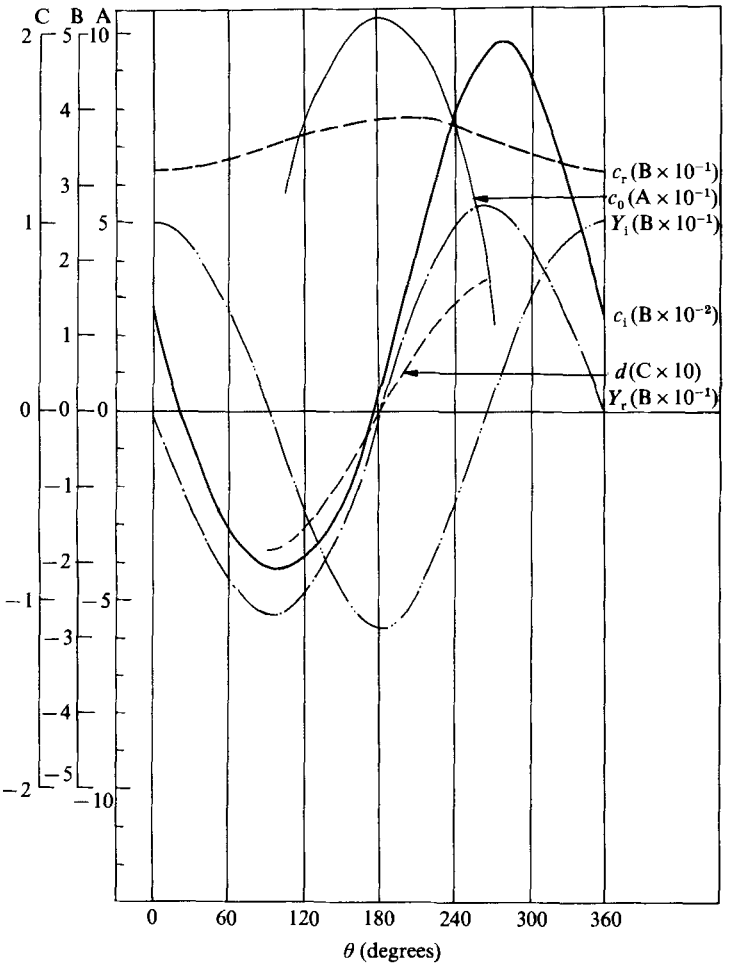

FIGURE 16. Back-calculated values of c_0 and d plotted versus θ, with $|\bar{\phi}_w| = 0.5$. Results are for the TS mode class.

unwieldy values of D (see (51)). In this way, part of the effect of the spring stiffness of the compliant layer was retained in the formulation. Typical sets of results are given in tables 1, 2 and 3.†

Figure 16 gives results for the TS mode class for $|\bar{\phi}_w| = 0.5$ with $m = 2$. The plots for the back-calculated values of c_0 and d immediately give us a reliable picture of the region in θ that is physically realizable, this being the region where both c_0 and d are positive. Actually when $c_0^2 > 0$ then a positive and a negative root of c_0 are obtained, representing respectively the downstream and upstream surface waves. However when $c_0^2 < 0$, no real value for c_0 is obtained. In figure 16 and in subsequent such figures, only the positive root of c_0^2 is plotted for $c_0^2 > 0$. It is seen in figure 16 that in the region where $Y_i > 0$ $c_0^2 < 0$ and thus this region is not physically realizable. Thus the zero-crossing of c_i close to $\theta \approx 0°$ is physically not realizable, whereas that close to $\theta \approx 180°$ is. For the latter, $c_0 \approx 1$ and $c_r \approx 0.3$–0.5. It may be seen from (49) that with a large separation between c_0 and c_r, d will follow Y_r in the region $c_i \approx 0$ (with $\theta \approx 180°$) and this is exactly what the figure reveals. Thus a few important and

† Tables 1, 2 and 3 are available from the authors or the Editor.

obvious conclusions may be drawn from the results. First that increase in d leads to destabilization and this is in line with Benjamin (1960) and Landahl's (1962) findings. Secondly that the neutral stability point for TS modes is near $\theta \approx 180°$. Thirdly, the physically realizable stable zone, when it exists, is very small in range (in θ) as compared to the unstable zone. Fourthly, in view of this third reason, small changes in the parameters of the compliant surface, or shifting to other points in the (α, R)-plane, can cause a near-neutral situation to easily change from stability to instability or vice versa, a fact that is responsible for the existence of so many different kinds of neutral curves for the TS modes in the earlier literature. Accordingly, with a typical set of values like $m = 2.0$, $c_0 = 1$ and $d = 0.01$, as chosen by Landahl (1962), one would hover around the region $c_i \approx 0, \theta \approx 180°$ in the entire (α, R)-plane, sometimes in the region when $c_i < 0$ and sometimes in $c_i > 0$. Thus, stabilization of TS modes poses a critical design problem and the best way to handle the situation, in our opinion, is not to try to stabilize the TS modes but to create conditions so that they do not exist.

The results also provide indirect confirmation of Landahl's (1962) and Benjamin's (1963) contention that the TS-modes are 'Class A', that is energy deficient, because, in the region near $c_i \approx 0, \theta \approx 180°$ in figure 16, it is seen that the addition of damping leads to destabilization.

The results at other points in the (α, R)-plane are broadly similar to the above, except that the points (0.03, 2500) and (0.4, 200), respectively for very low α and very low R, are so far removed from the rigid-wall neutral curve that the rigid-wall value for c_i at these points is already very large and negative. Thus in these regions the physically realizable stable region exists over a much larger range in θ. So in the pliable-wall case also, the stabilization of TS modes is not a problem either at very low α or at very low R, as in the rigid-wall case.

Next we consider the results for the KH mode class. The back-calculated c_0 and d are plotted in figure 17, with $m = 2$, $|\bar{\phi}_w| = 0.1$, $\alpha = 0.733$ and $R = 2562.8$. The first feature that strikes us is that the curves for Y_r and d do not follow each other even near the regions of $c_i \approx 0$. Thus physical realizability has to be ascertained based on the signs of c_0 and d. It is seen further that the zero-crossing of c_i near $\theta \approx 30°$ (i.e. nearer to $\theta = 0°$) is physically not realizable since this is in the region of $d < 0$. The other zero-crossing of c_i, near $\theta \approx 210°$ (i.e. nearer to $\theta = 180°$), is physically realizable. However, certain interesting and unexpected features are revealed for this region. It is seen that whereas c_0 is low as expected, having values of 0.1–0.5, and that c_r is of the order of c_0^2, unexpectedly the value of d is very high; being $d \sim 5$, $|\bar{\phi}_w| = 0.1$ to $d \sim 1, |\bar{\phi}_w| = 1.0$. Moreover, it is seen from the same figure that both c_0 and d are relatively stationary in the region $\theta \approx 210°$, that is in the region of (the physically realizable) $c_i \approx 0$. This feature makes the stability of these modes critically dependent on the values of c_0 and d for a given m, because once a mode is brought into existence, close to neutrality, then even slight changes in the values of c_0 and d could render the mode stable or unstable. Therefore, drift in values of c_0 and d, during operation, could also easily cause transition from stability to instability or vice versa, giving an impression that the system tends to stabilize or destabilize 'of its own' in a near-neutral situation.

The broad features of the mode (in the limited context of the region near $c_i \approx 0$ with $\theta \approx 210°$) make it appear that the mode could be the one found by Landahl (1962) which is 'Class B' for upstream-travelling and 'Class A' for downstream-travelling waves. Carpenter & Garrad (1986) have called this low-speed travelling wave flutter. However, the 'Class A' or 'Class B' features are not readily identifiable

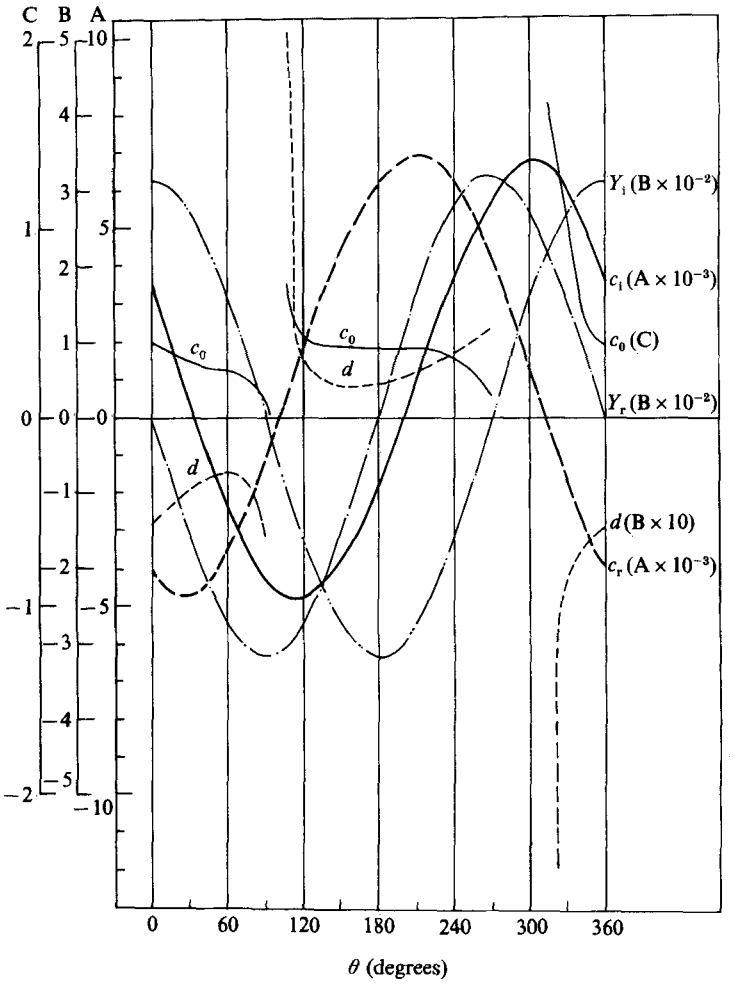

FIGURE 17. Back-calculated values of c_0 and d plotted versus θ, with $|\bar{\phi}_w| = 0.1$. Results are for the KH mode class.

from the present results. It seems that the plot for d near $c_i \approx 0, \theta \approx 180°$ has a minimum with a flattish bottom. And, 'Class A' and 'Class B' behaviour could be surmised to exist respectively along the right-side and left-side rising limbs in the plot for d. But again, for both these limits, $c_r > 0$, i.e. the waves travel downstream. The confluence of the two situations, i.e. the region of the flat minimum of d, seems therefore to show 'Class C' features, in which case the mode would seem to be closer to static divergence since c_r is small. It should be mentioned that the classification of static divergence by energy analysis is a tricky matter, as has been discussed in detail by Carpenter & Garrad (1986). Thus, owing to these somewhat conflicting details, we refrain from making any classification based on energy analysis. And as already discussed earlier herein, we term the mode class (i.e. the full 0°–360° loop in θ, and not the particular set of modes near $c_i \approx 0, \theta \approx 180°$) the KH mode class.

The curves in figure 17 reveal another interesting feature. It is seen that the curves for c_0 and d develop singularities across the zero-crossings of the c_r versus θ curves.

This can be explained from (49)–(51). It is seen that when c_r and c_i are small, and $c_r \to 0$, then from (50) c_0^2 is approximately given as

$$c_0^2 \approx -\frac{Y_i D}{c_r}, \tag{52}$$

where D is given by (51) and is always positive. Thus if $Y_i < 0$ at $c_r = 0$, then c_0^2 approaches $+\infty$ or $-\infty$ with the same sign as c_r as $c_r \to 0$, and with the opposite sign as c_r when $Y_i > 0$. Moreover, it is seen from (49) that though c_0^2 is large (which happens when $c_r \to 0$), Y_r has to remain bounded. Therefore D should also remain bounded. This gives

$$c_0^2 + c_i \frac{d}{\alpha} \approx 0. \tag{53}$$

Incidentally (53) also keeps the numerator of (49) bounded. Thus, for $c_r \to 0$, if $c_i < 0$ then $d \to \infty$ with the same sign as c_0^2, and if $c_i > 0$ then $d \to \infty$ with the opposite sign of c_0^2. Whereas this singular behaviour of c_0^2 and d is not of much significance for the regular KH modes, this is of great significance in the transitional modes.

The picture for the KH mode class at other points in the (α, R)-plane is similar. However, the points (0.03, 2500) and (0.4, 200), respectively for very low α and very low R, call for special mention. For such points the KH modes may be brought into existence for comparatively low values of d also, particularly for the points at low α. Nevertheless, except for the extreme regions of very low α and very low R, physically realizable KH modes can exist only for high values of d. Now, if Landahl (1962)-type values $m = 2.0$, $c_0 = 1$ and $d = 0.01$ are specified, then there would be no possibility of triggering KH modes in the (α, R)-plane except either at very low α or at very low R.

Next we consider the results for the resonant (R) mode class. Figure 18 gives the c_0 and d curves for $m = 2$ at $\alpha = 0.733$, $R = 2562.8$ for $|\bar{\phi}_w| = 24$. Immediately the reason for naming these 'resonant modes' becomes obvious, because the c_0 and c_r curves are of the same shape, with c_r being slightly less than c_0 everywhere. Moreover, it is seen from figure 18 that Y_r is small compared to Y_i, and Y_i has a large negative value. This is because for high values of $|\bar{\phi}_w|$ the integral in (11) is dominated mainly by the large value of $|\bar{\phi}_w|$. Thus with $\hat{p}_w$ mainly behaving as $\hat{p}_w \sim |\bar{\phi}_w|$, it is seen from (12) that the admittance Y will be dominated by a large negative Y_i in the entire range of θ.

For comparatively low values of $|\bar{\phi}_w|$ (≈ 7.0), it was found that the Y_r and d curves do not follow each other but, for higher values of $|\bar{\phi}_w|$ (see figure 18), the Y_r and d curves do follow each other. Moreover, it appears also that both the zero-crossings of c_i, one near $\theta \approx 0°$ and the other near $\theta \approx 200°$ (i.e. closer to $\theta = 180°$), are physically realizable, and that increase in the value of d stabilizes both these points of neutral stability. Thus there is a clear-cut 'Class B' feature observable in line with Landahl and Benjamin's findings.

Moreover, the entire region of $c_i < 0$ (approximately half the cycle of 0–360° in θ) is physically realizable, as this corresponds to the region $d > 0$ and $c_0^2 > 0$. Thus an important conclusion is that near-neutral disturbances for R modes are easily stabilized by the increase of damping. Two other points call for attention. First that for $c_i = 0$ near $\theta \approx 0°$, $c_r > 1$, and for $c_i = 0$ near $\theta \approx 180°$, $c_r < 1$. Thus, the neutral stability points for the R modes as reported by Landahl (1962), which were for $c_r < 1$,

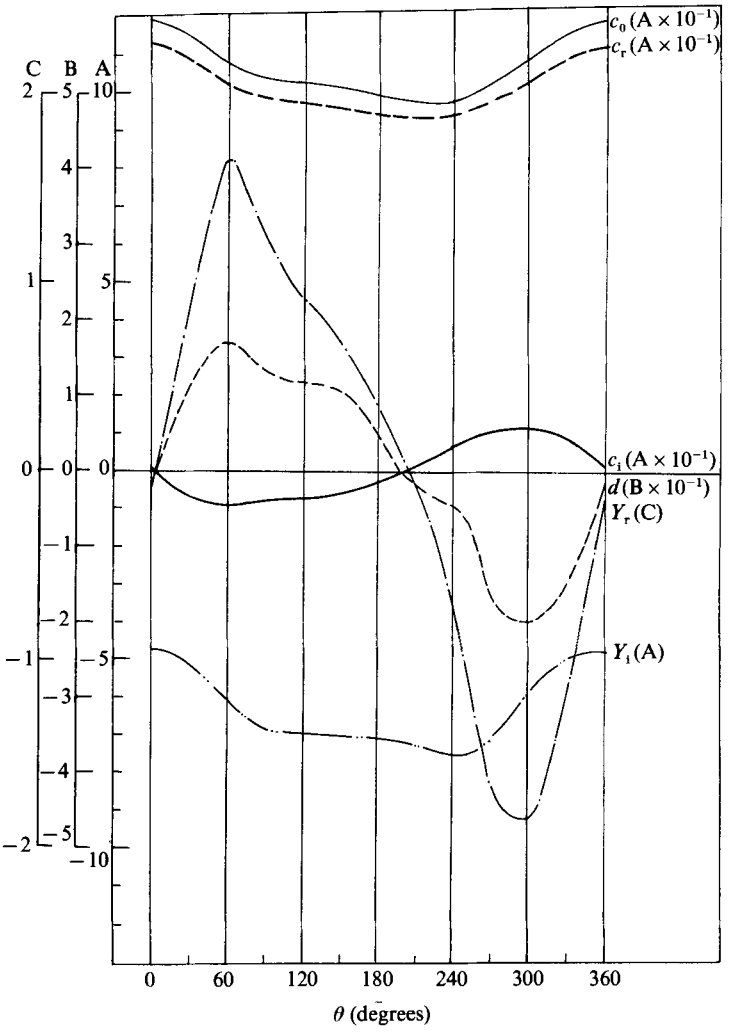

FIGURE 18. Back-calculated values of c_0 and d plotted versus θ, with $|\bar{\phi}_w| = 24$. Results are for the R mode class for a comparatively high value of $|\bar{\phi}_w|$.

actually belong to the region $\theta \approx 180°$. Secondly, we compare the behaviour of TS modes and R modes. It was seen for the TS modes that the entire region from $\theta \approx 180°$ to $\theta \approx 360°$ was physically realizable but with $c_i > 0$, i.e. *unstable*. And, sometimes a physically realizable 'stable pocket' could be found near $\theta \approx 180°$, for the narrow region in θ bounded by $c_i < 0$, $Y_r = 0$ and $c_i = 0$, $Y_r > 0$, whereas, for the R modes the entire region from $\theta \approx 0°$ to $\theta \approx 180°$ is physically realizable with $c_i < 0$, i.e. *stable*. Further, sometimes either near $\theta \approx 0°$ or near $\theta \approx 180°$, a physically realizable 'unstable pocket' can be found for a narrow region in θ bounded by $c_i = 0$, $Y_r > 0$ ($d > 0$) and $c_i > 0$, $d = 0$. An R-unstable pocket is shown in figure 19. Thus our conclusion is that when R-mode instability occurs one has moved into an R-unstable pocket, and when TS-mode stability occurs one has moved into a TS stable pocket. It is now seen by comparison how very difficult it is to stabilize the TS modes, when these modes exist.

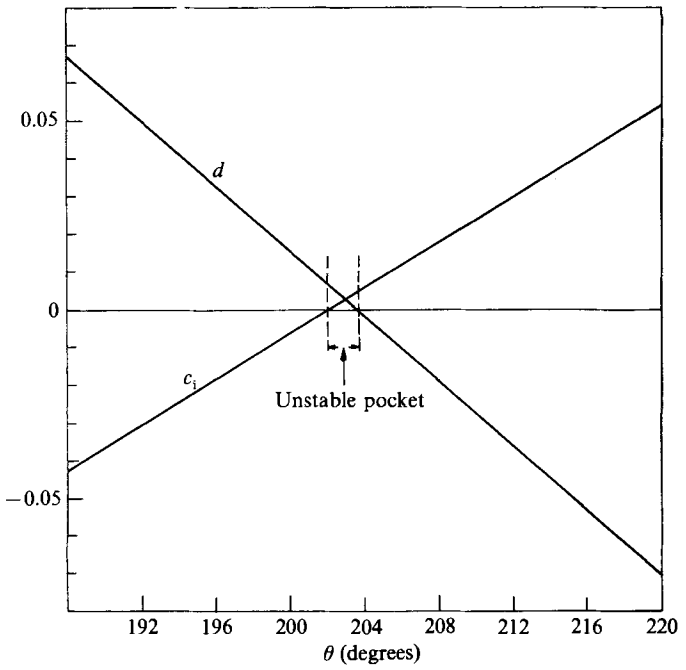

FIGURE 19. Curves for c_i and d versus θ, with an enlarged scale for θ in the range $188° \leqslant \theta \leqslant 220°$, for $|\bar{\phi}_w| = 10$. Results are for the R mode class and figure shows the existence of an 'unstable pocket'.

The behaviour of d, as shown in figure 18, may be deduced from (49)–(51). For the R modes it is known that $c_0^2 \approx c_r^2 \approx |c|^2$. Thus it is seen from (49) that

$$Y_r \approx \frac{|c|^2\left(2c_i + \dfrac{d}{\alpha}\right)}{D}, \tag{54}$$

where D is already small because $c_0^2 \approx |c|^2$. Thus for Y_r to remain bounded, $c_i \approx -d/2\alpha$, which incidentally renders D still smaller, as may be seen from (51). Moreover, it is seen from (50) that if Y_i is to remain bounded for small D, then $c_0^2 \approx |c|^2$, which is the main characteristic of the R modes. Also, since we know that $Y_i < 0$ for R modes (with large $|\bar{\phi}_w|$), it follows from (50) that $c_0^2 > c_r^2$. All these features are reflected in figure 18.

With Landahl-type values of $m = 2.0$, $c_0 = 1$ and $d = 0.01$, we see that it would not be difficult to land in an R unstable pocket for the R modes at some point in the (α, R)-plane. Thus the conflicting requirement on d, to be large in order to stabilize R modes and to be small in order to try to stabilize TS modes, makes it difficult to satisfactorily stabilize both over a wide range in the (α, R)-plane. In our opinion, effort should be directed to eliminate both these modes rather than to try to stabilize both.

The points in the (α, R)-plane at $(0.03, 2500)$ and at $(0.4, 200)$, respectively for low α and low R, did not show any major qualitative differences from the above, except that in both cases the zero-crossings in c_i moved closer to each other rather than being separated by approximately 180° in θ as earlier.

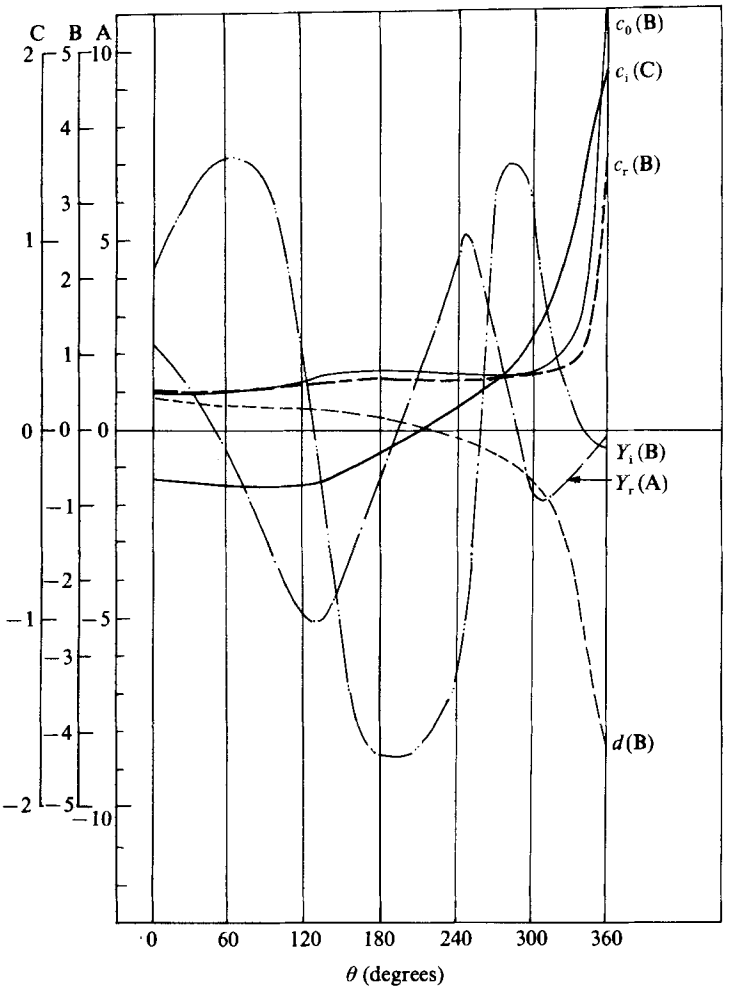

FIGURE 20. Back-calculated values of c_0 and d plotted versus θ, for the case $|\bar{\phi}_w| = 5(1)$. Results are for the transitional mode class corresponding to $|\bar{\phi}_w| = 5(1)$ as shown in figures 8 and 9.

We now take a quick look at two of the important transitional mode classes. Again the chosen point is at $\alpha = 0.733, R = 2562.8$, with $m = 2.0$. Figure 20 shows the mode class for which $c_r \to +\infty, c_i \to +\infty$, when $\theta \approx 360°$, with $|\bar{\phi}_w| = 5.0(1)$, i.e. for the first cycle of the $|\bar{\phi}_w| = 5.0$ curves in figures 8 and 9. Figure 21 shows the mode class for which $c_r \to -\infty, c_i \to +\infty$, when $\theta \approx 360°$, and this corresponds to $|\bar{\phi}_w| = 3.0(2)$ as shown in figures 8 and 9. It is seen from figure 20 that the transitional mode class for $|\bar{\phi}_w| = 5.0$ shows part R behaviour especially in the region $\theta \approx 180°$ to $\theta \approx 360°$. The value of c_r about 0.5 for $\theta = 180°$. Thus, the R modes at comparatively low values of c_r that were found by Landahl (1962) and others do not belong to the regular R mode class but to the transitional mode class. Fortunately this mode class is not very dangerous because mostly where $c_i > 0, d < 0$, it is not physically realizable. However, it is possible to obtain an unstable pocket of the R-mode type near $\theta \approx 180°$, but such a pocket is easily stabilized by increasing the damping d. Moreover, this type of transitional mode is not found for values of c_r very much lower than $c_r \approx 0.5$. For lower values of c_r this type of transitional mode is replaced by the other

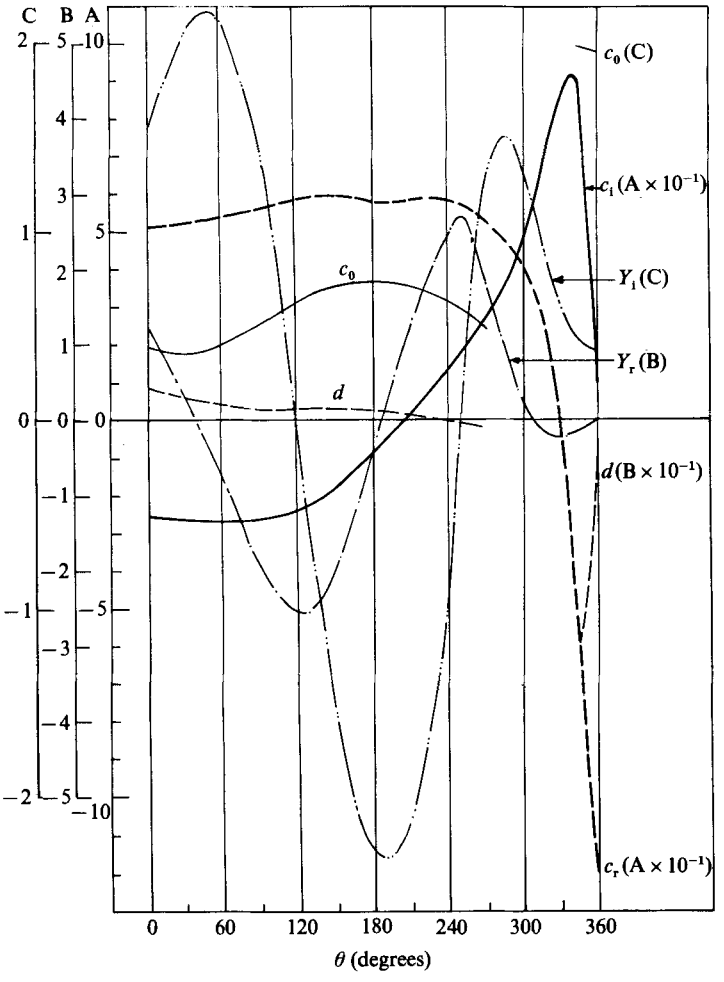

FIGURE 21. Back-calculated values of c_0 and d plotted versus θ, for the case $|\bar{\phi}_w| = 3.0(2)$. Results are for the transitional mode class corresponding to $|\bar{\phi}_w| = 3.0(2)$ as shown in figures 8 and 9.

shown in figure 21. Therefore, R-mode-type behaviour, even from a transitional mode class, is not expected at values of c_r very much lower than $c_r \approx 0.5$.

Next we look at the other transitional mode class shown in figure 21, for $|\bar{\phi}_w| = 3.0$. Here, since $c_r \to -\infty, c_i \to +\infty$, when $\theta \approx 360°$, there is a zero-crossing of c_r near $\theta \approx 330°$, and the associated singularity of c_0^2 and d at $c_r = 0$. The behaviour of this mode class in the region $\theta \approx 180°$ to $\theta \approx 360°$ is in part similar to that of KH-type modes at very low values of α. The left-side of the point of zero-crossing of c_r in figure 21, where both c_0 and d could be small and positive, and where c_i is very large and positive, could be a very dangerous physically realizable unstable zone. This point will be further discussed in §9.

9. Concluding remarks

Various conclusions drawn from this study have already been mentioned at the appropriate stages in the text. The major conclusions are that there are essentially three important mode classes: viz. TS, KH and R mode classes, and also two

important transitional mode classes. The results for the TS and R mode classes agree with those of earlier workers. However it is difficult to classify the KH mode class based on earlier work. Two important concepts evolve in connection with the TS and R mode classes, namely the existence of stable pockets for the TS mode class and unstable pockets for the R mode class. For both mode classes, approximately half the cycle in 0–360° of θ is physically realizable. But, for the TS mode class most of the physically realizable range is unstable with an occasional small stable pocket. And, for the R mode class most of the physically realizable range is stable with an occasional unstable pocket. Whereas the addition of damping stabilizes R modes it destabilizes TS modes. These conflicting requirements make it difficult to simultaneously stabilize both TS and R modes in the entire (α, R)-plane.

In looking for a possible clue to a satisfactory stabilizing coating based on the present results, we recall our conclusion that both the TS and R modes (regular as well as transitional) should be altogether avoided rather than stabilized. Figures 16–21 show that it is possible to achieve this by keeping the value of c_0 as low as possible, that is $c_0 \approx 0.25$. Very low values of c_0, however, make it difficult for the compliant surface to bear the static loading and so a compromise has to be effected. Along with a low value of c_0, a low value of $d \leqslant 0.05$ has also to be maintained so that the unstable (regular) KH modes are eliminated as well, except at very low values of α. The value of m may be kept in the range $m = 1$ to 2. Careful investigation shows that except for the transitional mode discussed in figure 21, all other modes are either stable or physically non-existent when c_0 and d are small. Indeed we ran a pilot survey of the (α, R)-plane with $m = 1.0$, $c_0 = 0.1$ and $d = 0.001$, which showed that all the regular TS and R modes were stable or non-existent even up to $R = 8000$. However, a persistent instability was observed at various points somewhat below the lower limb of the rigid-wall neutral curve. A typical such point is at $\alpha = 0.4$ and $R = 3000$. We checked that this instability was exactly of the type depicted in figure 21. The scheme for stabilization suggested herein seems to be a good compromise. At least one departure from past effects is made in that it is suggested that the TS modes and R modes should be avoided rather than stabilized. Our results are, however, unable to explain Kramer's. However, Carpenter & Garrad (1985) were able to demonstrate a reduction in the growth rate of TS waves in a Kramer-type surface.

We would like to mention an important experimental result of Babenko & Kozlov (1973), referred to by Carpenter & Garrad (1985). It appears that Babenko & Kozlov experimentally studied the stability of flow past a compliant surface made of polyurethane foam with and without a tensioned membrane. The best results were obtained for a flat strip of polyurethane foam without a tensioned membrane. This way the critical Reynolds number was approximately doubled and the amplification rate halved, as compared to the rigid-wall case. The addition of a tensioned membrane increased the region of instability compared to the rigid wall. If we compare Babenko & Kozlov's results with the present theoretical results we find a good measure of consistency. The absence of a tensioned membrane, and the soft structure of polyurethane foam, keep the value of c_0 small. Also, in its rubbery state at ordinary temperatures, this material has a low value of d.

We now offer some comments on negative damping. It is seen that if c_0 is kept small (≈ 0.25 or so) and d has a small negative value, of the order $d = -0.1$ to -0.2, then all the earlier mentioned advantages are retained and, in addition, the contingency leading to instability as in figure 21, or for the low α KH modes, is

avoided. Instead, as may be seen from figure 17, regular KH modes may exist but only in the damped region $c_i < 0$ at values of θ that are less than at the first zero-crossing of c_r in the 0°–360° cycle of θ. Mathematically therefore, a negative value of d along with a comparatively small value of c_0 offers a very interesting possibility of stabilization, first by excluding the TS and R modes and secondly by allowing KH modes to exist only in the damped region. The natural question that follows is whether an aquatic animal like a dolphin can simulate negative damping, and whether a manmade compliant surface can in future be made to do so. Both questions are outside the scope of this paper, but we outline what may possibly be entailed in the simulation of negative damping. Carpenter & Garrad (1985) have shown that the fluctuating pressure p_s of the substrate fluid behaves like a conventional damping term when the substrate depth is small. Thus, were it to be possible to sense this fluctuating pressure and simultaneously generate and superpose, by a feedback mechanism, a fluctuating pressure that is larger in magnitude than p_s but of opposite sign, then the overall effect would be to simulate negative damping. Whether a dolphin does this or not, to 'shake off' the instabilities, one cannot say at this stage, but the present results build a case to follow up such a conjecture. Recently, progress has been made in the study of stabilization by active surfaces, cf. Metcalfe *et al.* (1986), and others.

We are grateful to Professor J. T. Stuart of Imperial College, London, Professor M. Gaster of the University of Cambridge and Dr P. W. Carpenter of the University of Exeter for many valuable suggestions and encouragement.

REFERENCES

Babenko, V. V. & Kozlov, L. F. 1973 Experimental investigation of hydrodynamic stability on rigid and elastic damping surfaces [in Russian]. *Ivz. Akad. Nauk. SSSR, Mekh. Zhid. i Gaza* no. 1, 122–127.

Benjamin, T. B. 1959 Shearing flow over a wavy boundary. *J. Fluid Mech.* **6**, 161–205.

Benjamin, T. B. 1960 Effects of a flexible boundary on hydrodynamic stability *J. Fluid Mech.* **9**, 513–532.

Benjamin, T. B. 1963 The three fold classification of unstable disturbances in flexible surfaces bounding inviscid flows. *J. Fluid Mech.* **16**, 436–450.

Carpenter, P. W. & Garrad, A. D. 1985 The hydrodynamic stability of flow over Kramer-type compliant surfaces. Part 1. Tollmien–Schlichting instabilities. *J. Fluid Mech.* **155**, 465–510.

Carpenter, P. W. & Garrad, A. D. 1986 The hydrodynamic stability of flow over Kramer-type compliant surfaces. Part 2. Flow-induced surface instabilities. *J. Fluid Mech.* **170**, 199–232.

Hains, F. D. 1965 Preliminary results on boundary-layer stability on a flexible plate. *AIAA J.* **3**, 775.

Korotkin, A. I. 1965 The stability of a laminar boundary layer on an elastic surface in an incompressible fluid (in Russian). *Izv. Akad. Nauk. SSSR, Mekh. Zhid. i Gaza* no. 3, 38–44.

Kramer, M. O. 1957 Boundary-layer stabilization by distributed damping. *J. Aero. Sci.* **24**, 459.

Kramer, M. O. 1960*a* Boundary-layer stabilization by distributed damping. *J. Am. Soc. Naval Engrs* **72**, 25–33.

Kramer, M. O. 1960 The dolphin's secret. *New Scientist* **7**, 1118–1130.

Kramer, M. O. 1965 Hydrodynamics of the dolphin. *Adv. Hydrosci.* **2**, 111–130.

Landahl, M. T. 1962 On the stability of a laminar incompressible boundary layer over a flexible surface. *J. Fluid Mech.* **13**, 609–632.

LANDAHL, M. T. & KAPLAN, R. E. 1965 Effect of compliant walls on boundary layer stability and transition. *AGARDograph* 97-1-353.

METCALFE, R. W., RUTLAND, C. J., DUNCAN, J. H. & RILEY, J. J. 1986 Numerical simulations of active stabilization of laminar boundary layers. *AIAA J.* **24**, 1494–1501.

SCHLICHTING, H. 1968 *Boundary Layer Theory*, 6th edn. McGraw-Hill.

THOMAS, L. H. 1953 The stability of plane-Poiseuille flow. *Phys. Rev.* **91**, 780–784.